

https://dspace.org/

Blast wave generation and interactions

Chirewa, B.T.

2024
https://hdl.handle.net/10539/37393

Downloaded from a DSpace repository. https://dspace.org/

Blast Wave Generation and interactions

B.T. Chirewa

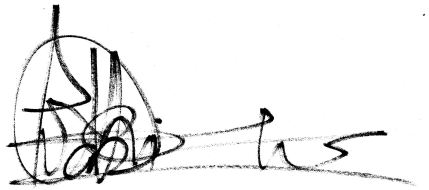
A dissertation submitted to the Faculty of Engineering and the Built Environment, University of the Witwatersrand, Johannesburg, in fulfilment of the requirements for the degree of Master of Science in Engineering.

Johannesburg, April 2022

Declaration

I declare that this dissertation is my own, unaided work, except where otherwise acknowledged. It is being submitted for the degree of Master of Science in Engineering in the University of the Witwatersrand, Johannesburg. It has not been submitted before for any degree or examination at any other university.

Signed this 19th day of April 2022



B.T. Chirewa

I would like to dedicate this dissertation to my mother. I love you mom. I wish you were here to see how far your boy has come.

Acknowledgements

I would like to thank my distinguished supervisor, Professor Beric W. Skews for his continuous support and guidance throughout the course of this study.

I would like to thank Doctor Randall T. Paton and Sabrina Myburgh for their assistance and advice throughout my experimentation and numerical simulations.

I would like to thank the staff of the North West Engineering workshop for their assistance with the technical expertise.

I would like to thank my aunt, Gertrude Chirewa, for her emotional support, prayers and motivation throughtout the duration of my studies.

Lastly but certainly not least, I would like to thank my father for his support and guidance throughout my education.

Abstract

The purpose of this study was to produce blast waves and study the flow properties behind the blast wave wherre the blast wave Mach number ranges from 1.11 to 1.44. Previous studies on blast waves only focused on the positive phase of the pressure decay profile. The negative phase is usually ignored. The negative phase was given more attention in this study. A blast tube that was designed in a previous study was used in the experiments to generate the blast waves. A numerical study was performed using Ansys CFD software alongside the experimental study to have a validation for the blast tube design. Both the experimental and the numerical pressure decay profiles showed strong correlation with the Friedlander pressure decay profile. The decay profiles were further validated by calculating the positive impulse. This was calculated as the area under the positive phase of the decay profiles. The experimental positive impulse was 1.08% higher than the positive impulse of the Friedlander profile and the numerical positive impulse was 1.32% higher than the positive impulse of the Friedlander profile. These were insignificant differences which showed that the blast tube was producing blast waves of good quality. The secondary shock was observed in the pressure traces as a sharp increase in pressure in the negative phase followed by a gradual decrease. It was noted that the secondary shock wave remained in the negative phase. The flow velocity in the negative phase was observed to be high enough to pick debris caused by the incident shock wave which can result in further structural damage. As the Mach number increases, the incident shock wave and the secondary shock wave become further apart. This is because the speed of the incident shock wave increases at a faster rate with increasing Mach number than the speed of the secondary shock wave. The experimental diffraction was studied on a 90° corner using a schlieren optics setup connected to a high-speed camera set to capture 65000 frames per second. The observed diffraction patterns in the perturbed region were similar to those observed in the diffraction of weak shock waves. This region was characterised by a diffracted shock wave, a reflected expansion wave, a vortex, a slipstream and a viscous vortex. The slipstream angle was noted to decrease during the blast wave diffraction, contrary to shock wave diffraction where the flow is pseudo-stationary. The contact surface that is seen in the diffraction of weak shock waves was observed being entrained into the vortex but not visible near the incident shock wave. The reflected expansion wave that is circular in

the diffraction of weak shock waves was seen to be distorted in the blast waves case. The distortion happened as soon as it encountered the variable velocity and sound speed behind the incident shock wave. A comparison of the ratio of the distance moved by the expansion wave to the distance moved by the incident shock wave during diffraction was made between normal shock waves and the blast waves. It was observed that the ratio was higher for blast waves than for shock waves. This is because the flow velocity trailing a blast wave decreases at a faster rate than the decrease in sound speed. This causes the reflected expansion wave to propagate further upstream in blast wave diffraction than in shock wave diffraction. The difference between the ratios was observed to become smaller as the Mach number approaches unity. This was because flow velocity tends to zero at Mach 1 and the propagation of the reflected expansion wave will only be determined by the sound speed which will be similar for both the blast wave diffraction and the shock wave diffraction. A higher resolution camera should be used to allow for accurate measurement of distances and a wider range of Mach numbers should be used to confirm the trend. A numerical study with better flow visualisation resources is recommended for future studies. Future studies are also recommended on the vortex behaviour in blast wave diffraction, which was established to be much more complex than in shock wave diffraction.

Contents

Declaration **i**

Acknowledgements **iii**

Abstract **iv**

Contents **vi**

List of Figures **x**

List of Tables **xiii**

List of Symbols **xiv**

1 Introduction **1**

1.1 Research Background 1

1.2 Research Motivation 2

1.3 Research Aim 2

1.4 Research Assumptions 3

2 Literature Survey **4**

2.1 Introduction to Gas Dynamics 4

2.2 What is a blast wave? 4
2.2.1 The blast wave decay parameter 5
2.2.2 Blast wave impulse 6
2.3 Explosive generation of blast waves 6
2.4 Shock waves and Blast Waves 6
2.5 Expansion waves and the secondary shock wave 9
2.6 Non-explosive generation of blast waves 11
2.7 Interactions of Shock waves 12
2.7.1 Diffractions 12
2.8 Flow visualisation 13
2.8.1 Shock Waves Visualisation 13
2.9 Shock Wave strength 15

3 Research objectives **16**

4 Research apparatus **17**

4.1 Experimental apparatus 17
4.1.1 Blast tube 17
4.1.2 Schlieren setup 19
4.2 Numerical study 20
4.2.1 Geometry 20
4.2.2 Meshing 21
4.2.3 Solver settings 22

5 Methodology **26**

5.1 Experimental 26

5.1.1 Compressed air storage 26

5.1.2 Pre-Testing Procedure 27

5.1.3 Blast Tube Testing Procedure 27

5.1.4 Blast Tube Shut Down Procedure 28

5.1.5 Precautions 29

5.2 Flow Visualisation 30

6 Observations **31**

6.1 Experimental data 31

7 Data Processing **34**

7.1 Mach Number Calculation 34

7.2 Pressure traces 35

7.3 Positive Impulse 36

7.4 Image Processing 37

8 Results and Discussion **38**

8.1 Pressure Traces 38

8.1.1 Experimental pressure trace vs Friedlander 38

8.1.2 Experimental pressure trace vs CFD 42

8.1.3 CFD pressure trace vs Friedlander 44

8.1.4 Positive Impulse 46

8.1.5 Decay time and second shock time 47

8.2 Diffraction 48

8.2.1 Experimental 48

8.3 Blast wave vs shock wave diffraction 51

9 Conclusions **56**

10 Recommendations **58**

References **59**

A Unprocessed Images **61**

B Matlab codes **62**

List of Figures

2.1 Blast wave pressure - time decay profile adapted from Friedlander (1946) . . 5

2.2 Propagating shock wave in a shock tube 8

2.3 Shock wave properties 8

2.4 Streak image of bursting glass sphere. Glass (1974). 9

2.5 simplified blast tube geometry 11

2.6 Incident shock wave moving towards a 90 degree corner. 13

2.7 Perturbed region behind a low Mach number diffracting shock wave adapted from B. Skews et al. (2012) 13

2.8 The optical setup for the shadowgraphy technique G. Settles (2002) 14

2.9 The optical setup for the schlieren flow visualisation technique adapted from G. S. Settles and Hargather (2017) 14

4.1 Schematic of the blast tube 18

4.2 Schlieren setup used in the experiment 19

4.3 Driver section of the blast tube modelled in SolidWorks 20

4.4 Imported blast tube geometry shown in Tecplot 21

4.5 The mesh settings for the CFD model 21

4.6 The mesh settings for the CFD model 22

4.7 The mesh settings for the CFD model 22

4.8 The mesh settings for the CFD model 23

4.9 The meshed driver section 23

6.1 Unprocessed oscilloscope pressure trace 33

7.1 Image after processing 37

8.1 Experimental pressure trace vs Friedlander pressure trace 38

8.2 Experimental trace vs Friedlander pressure profile at Mach 1.11 39

8.3 Experimental trace vs Friedlander pressure profile at Mach 1.17 39

8.4 Experimental trace vs Friedlander pressure profile at Mach 1.20 40

8.5 Experimental trace vs Friedlander pressure profile at Mach 1.24 40

8.6 Experimental trace vs Friedlander pressure profile at Mach 1.27 41

8.7 Experimental trace vs Friedlander pressure profile at Mach 1.31 41

8.8 Experimental trace vs Friedlander pressure profile at Mach 1.34 42

8.9 Experimental trace vs Friedlander pressure profile at Mach 1.35 42

8.10 Experimental trace vs Friedlander pressure profile at Mach 1.37 43

8.11 Experimental trace vs Friedlander pressure profile at Mach 1.44 43

8.12 Experimental pressure trace vs CFD pressure trace 44

8.13 Friedlander pressure trace vs CFD pressure trace (Mach 1.24) 44

8.14 Experimental pressure trace vs Friedlander pressure trace vs CFD pressure trace 45

8.15 Positive impulse calculated from normalised pressure decay profiles (Mach 1.24). 46

8.16 Pressure decay profiles for various Mach numbers 47

8.17 Normalised pressure decay profiles for various Mach numbers 48

8.18 Time between incident shock and second shock 49

8.19 Blast wave diffraction around a 90 degree corner for test 5. (Mach 1.35) . . . 50

8.20 Blast wave diffraction around a 90 degree corner at different Mach numbers . 51

8.21 Distorted shape of reflected sound wave 53

8.22 Ratio of distance moved by expansion wave to distance moved by incident shock wave from the corner apex 53

8.23 Variation of sound speed and flow velocity behind the blast wave (Mach 1.24 nominal) 54

8.24 Variation of sound speed and flow velocity behind a normal shock wave with increasing Mach number 54

8.25 Velocity of blast wind at 1m distance from diaphragm 55

A.1 Image before processing 61

List of Tables

4.1 Calibration data for the pressure transducers that were used in the experiment 18

6.1 Experimental data 32

6.2 Pressure transducer peak voltages 32

7.1 Processed experimental data 35

7.2 Pressure transducer peak pressures 36

List of Symbols

β	Blast wave decay parameter
γ	Ratio of specific heats
c	Speed of sound in air
d_t	Distance between transducers
M	Shock wave Mach number
P_0	Blast wave peak overpressure
P_{atm}	Atmospheric pressure
R	Universal gas constant
T	Absolute temperature
t_a	Blast wave arrival time
t_d	Blast wave decay time
v	Shock wave speed
I_b	Blast wave impulse
P_0	Peak overpressure
V_{ch1}	Voltage from channel 1
V_{ch2}	Voltage from channel 2
CFD	Computational fluid dynamics
DS	Diffracted shock wave
IS	Incident shock wave
SL	Slipstream

TNT Trinitrotoluene

V Vortex

VV Viscous Vortex

Chapter 1 Introduction

This study will seek to generate blast waves with good visual quality and good Friedlander pressure decay profiles using non-explosive methods and to establish the effect of expansion waves in two-dimensional diffraction of blast waves. The blast waves that will be used for this study will be produced using the non-explosively driven blast tube designed by Demby (2018). Iterations and/ or modifications will be made to the blast tube design in terms of the filling mechanism to resolve the issues that were encountered by Demby in their design.

1.1 Research Background

Previous studies on blast waves focused on the positive phase only. The negative phase was given little to no attention. The blast tubes used in previous studies were designed to match the positive phase only. This study uses a tube that was designed to produce a negative phase and a second shock so as to mimic all features of an actual chemical or nuclear explosion. Demby (2018) settled on a non-explosively driven blast tube design consisting of a linearly diverging driver section fitted inside a pressure vessel. The driver section was then filled from the pressure vessel by means of a direct loaded poppet valve. The problem that arose with the design filling mechanism was the poppet valve opening during testing and allowing high pressure air into the driver section. This disrupted the formation of blast waves and this resulted in a diminished quality of the blast waves pressure decay profiles. Demby (2018) also encountered a problem of blast waves reflecting off the end of the tube and returning to prevent the full development of the blast wave profile and the detection of the secondary shock wave.

1.2 Research Motivation

Studies into interactions and propagation of blast waves are of great importance in the defence, mining, chemical and aerospace industries. In the defence industry understanding diffraction of blast waves will help in the design of effective weapons and defence vehicles that can withstand blast impact. In the mining industry this will be useful for the confinement of mining explosions for the health and safety purposes of the miners and the communities surrounding the mines. In the chemical industry understanding blast waves is essential for the containment of explosive reactions. In aerospace, blast waves arise in hypersonic velocity impact and sonic boom (Brode (1959)). All these call for understanding of blast waves in terms of how they interact with various surfaces. There is also no published work to date on two-dimensional diffraction of blast waves and the effect of the associated expansion waves. Previous studies on blast waves only focused on the positive phase of the pressure decay profile. The negative phase is usually ignored. However, the negative phase velocity can be high enough to pick up debris which can cause structural damage. The pressure in the negative phase can also cause cavities on biological material. The negative phase will an additional the focus of this study.

1.3 Research Aim

The aim of this study was to :

- produce blast waves with good visual quality and good Friedlander pressure decay profiles using non-explosive methods.
- study the development of secondary shock waves.
- study the perturbed region behind a blast wave diffracting around a 90° corner
- establish the effect of expansion waves in the diffraction of blast waves

Modifications and validation of the current blast tube will be required on the pressure filling mechanism to improve on the quality of the generated blast waves. Validation will be deduced from how closely their pressure decay profile matches with predictions of the Friedlander equations. Once the validation of the blast tube is completed, the study will continue to look into diffraction of blast waves around a 90° corner . The diffraction patterns observed in the diffraction of blast waves will be compared to the diffraction patterns observed in the diffraction of shock waves.

1.4 Research Assumptions

The working fluid in this study is air. It will be assumed that air behaves as an ideal gas. The properties of an ideal gas are as follows:

- The gas particles have negligible volume.
- The gas particles are equally sized and do not have inter-molecular forces (attraction or repulsion) with other gas particles.
- The gas particles move randomly in agreement with Newtons Laws of Motion.
- The gas particles have perfect elastic collisions with no energy loss therefore the internal energy of an ideal gas is only a function of temperature.

A viscous flow model will be assumed to model the flow in numerical analysis. This assumption is necessary to correctly model the boundary layer that develops near the walls. The initial flow of air will be assumed to be one-dimensional. This is fluid flow where all the streamlines of the flow are parallel to each other. The flow characteristics will remain constant in a direction perpendicular to the flow. This assumption will allow for the initial conditions of the blast waves to be determined.

Chapter 2 Literature Survey

2.1 Introduction to Gas Dynamics

Fluid flows are usually treated as incompressible when the Mach number (M) is less than 0.3. Incompressible flow is a type of fluid flow where the density of the fluid remains constant when the pressure of the fluid changes. In cases where the Mach number is greater than 0.3 then the flow is treated as a compressible flow. Compressible flow results in a change in fluid density when the applied pressure changes. When the fluid is compressed, the fluid density will increase and when the fluid is expanded the fluid density will decrease.

2.2 What is a blast wave?

A blast wave is characterised by a leading shock wave and a following exponential decay of air properties (pressure, temperature and density). A shock wave is a sudden increase in air properties. A shock wave is caused by an explosion or by a body moving faster than the speed of sound.

The sudden increase in pressure is because of a leading shock wave that is produced during the explosion. The gradual decrease in pressure is as a result of expansion waves trailing the leading shock wave.

The pressure (P) in a blast wave is shown in Figure 2.1.

This pressure-time decay profile is described by the Friedlander equation, named after its creator Friedlander (1946). This is shown in Equation 2.1, where P_0 is the blast wave over-pressure. This is the pressure caused by the leading shock wave. The result of Equation 2.1 is shown in Figure 2.1. The overpressure will be followed by an exponential decay which reaches ambient pressure P_{atm} in a decay time t_d. The region when the pressure is above

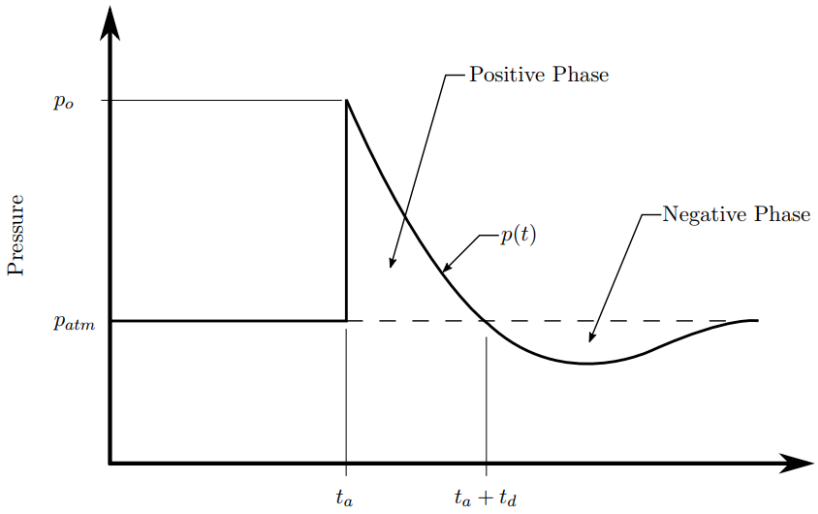


Figure 2.1: Blast wave pressure - time decay profile adapted from Friedlander (1946)

ambient pressure is called the positive phase. The pressure decay overshoots below the ambient pressure and then gradually rises back to ambient pressure. This is called the negative pressure phase (Friedlander (1946)).

$$P = P_0 e^{\frac{-t}{t_d}} \left(1 - \frac{t}{t_d}\right) \tag{2.1}$$

In cases where the peak overpressure (P_0) is greater than 1bar, the Friedlander equation given by Equation 2.1 will no longer be as accurate in describing the pressure decay profile behind the blast wave. In these cases, the modified Friedlander equation is used, this is shown in Equation 2.2. The modified Friedlander equation contains a blast decay parameter, β.

$$P = P_0 e^{\frac{-\beta t}{t_d}} \left(1 - \frac{t}{t_d}\right) \tag{2.2}$$

2.2.1 The blast wave decay parameter

The blast decay parameter has several formulations in literature that were determined empirically. The decay parameter β can be calculated from Equation 2.3 for $1bar < P_0 < 3bar$.

$$\beta = \frac{1}{2} + P_0 \left[1.1 - (0.13 + 0.2P_0)\frac{t}{t_0}\right] \tag{2.3}$$

The decay parameter β is essential for determining a more accurate pressure-time decay profile. The decay parameter also affects the decay time t_d which gives the length of the positive pressure phase. The length of the positive pressure phase affects the blast wave impulse (Karlos, Solomos and Larcher (2016)).

2.2.2 Blast wave impulse

The blast wave impulse is the total force per unit area that is applied to a structure during an explosion. This can be calculated as the area under the pressure time decay profile for the positive phase.

The blast wave impulse caused by the positive pressure region is the one that has a major contribution to structural damages that occurs during an explosion. The impulse in the negative pressure is usually not considered to be significant in structural analysis. This is because the peak pressure in the negative pressure phase is much less than the peak pressure in the positive pressure region (Goel et al. (2012)).

The blast wave impulse, (I_b) for the positive pressure phase is given by Equation 2.4. This is the area under the pressure-time decay profile from the time t_a to time t_d.

$$I_b = \int_{t_a}^{t_a+t_d} P(t)dt \tag{2.4}$$

When equation Equation 2.4 is solved it gives Equation 2.5.

$$I_b = \frac{P_0 t_d}{\beta}\left[1 - \frac{(1-e^{-\beta})}{\beta}\right] \tag{2.5}$$

2.3 Explosive generation of blast waves

Blast waves for research purposes can be generated using explosives such as Trinitrotoluene (TNT). Using TNT poses several safety risks and the explosion fragments disrupt the instrumentation for measuring pressure. This creates a challenge in studying blast waves thus there has been very few experimental studies on blast waves. Dewey (1964) is one of the few studies that uses TNT in their experimentation to study the air velocity in blast waves resulting from TNT explosions. Many studies on blast waves are carried out numerically. Brode (1958) describes a blast wave from the detonation of TNT based on a numerical calculation.

2.4 Shock waves and Blast Waves

Figure 2.2 shows a shock wave propagating in a shock tube. When a diaphragm bursts the shock wave is moves to the right, the expansion waves initially moves to the left, they reflect off the end of the tube and start to trail the shock wave and catch up with it. The trailing

expansion waves cause a reduction in the air properties of the trailing flow. That is air density, air temperature and air pressure. The trailing expansion waves cause the decaying pressure profile (Cullis (2001)).

A shock wave and a blast wave differ in their pressure-time profiles. The pressure-time profile for a shock wave is shown in Figure 2.3. The pressure decay is not immediate like the blast wave decay profile shown in Figure 2.1.

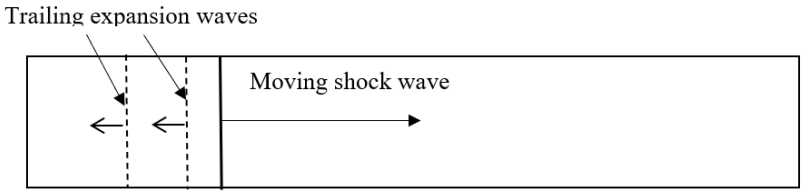


Figure 2.2: Propagating shock wave in a shock tube

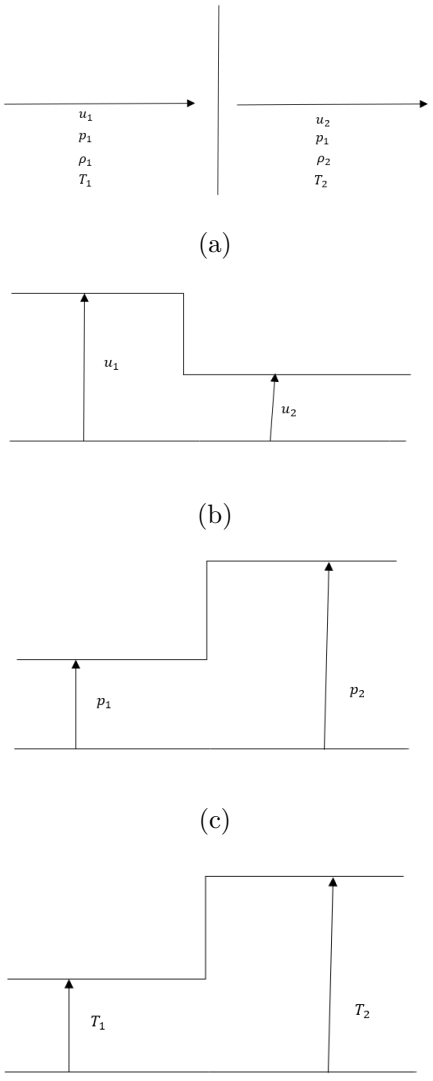


Figure 2.3: Shock wave properties

2.5 Expansion waves and the secondary shock wave

The secondary shock wave is mainly encountered in chemical explosions and spherical explosions.Figure 2.4 shows a streak image of a bursting glass sphere. S_1 is the incident shock wave and S_2 is the secondary shock wave. During an explosion, as the leading shock front of the blast wave propagates outwards from the center of the explosions, it leaves expanded trailing flow. This induces expansion waves which travel towards the center of the explosion. This results in a reduction in the air properties of the trailing flow (density, temperature and pressure). When the expansion waves implode at the center, extremely low temperatures, densities and pressures results in the gas which is then equalised by the formation of a reflected shock wave. This shock wave then propagates outwards from the center of the explosion. It is seen after the blast wave as a secondary shock wave (Brode (1959)).

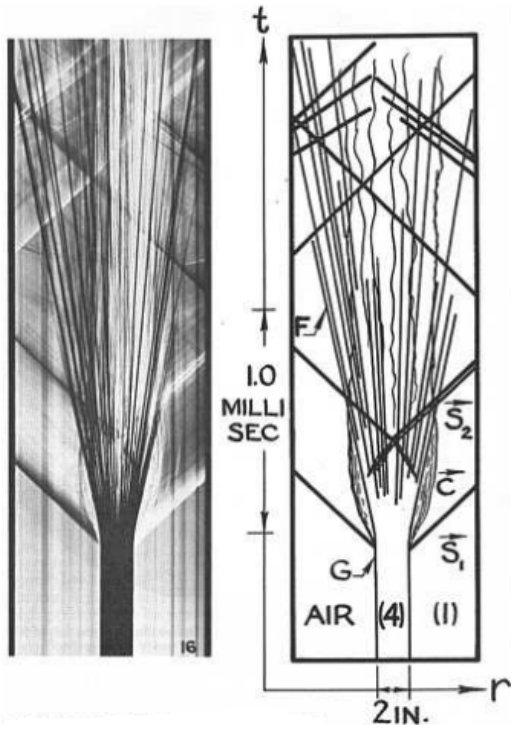


Figure 2.4: Streak image of bursting glass sphere. Glass (1974).

There is scarce literature on this phenomenon. This is because of the difficulty encountered in detecting the secondary shock in explosive generated blast waves. In explosive generated blast waves, the pressure measuring instrumentation records the blast wave that is reflected from the ground into the atmosphere as well as being obscured by explosion products and smoke and thereby affecting the detection of the secondary shock wave. However, the secondary shock is detected through pressure measurements by transient pressure gauges.

A number of recent studies have focused on traumatic brain injury (TBI) caused from exposure to an explosion. Taylor and Ford (2009) studied a tissue material model of a human head on exposure to simulated blast waves. They concluded that the primary cause of injury occurred at a shorter timescale than expected and before the onset of rotational and translational accelerations that are usually associated with traumatic brain injury. This shows the importance of blast waves studies.

Most studies usually neglect the flow properties in the negative phase. This is because considering the positive phase is usually considered a more conservative approach since the loads created in the negative phase are of much lesser magnitude than the loads created in the positive phase. However, in biological material such as brain tissue, the negative phase could cause cavitation. Goeller et al. (2012) showed that cavitation in biological material exposed to blasts impact coincided with periods of negative pressure.The negative phase is also associated with blast wind reversal. This results in a reversal in aerodynamic drag on aerodynamic structures which will in turn affect the aerodynamic loading. This shows that blast wave studies should consider the negative phase.

2.6 Non-explosive generation of blast waves

The non-explosive blast tube designed by Demby (2018) showed the ability to produce the secondary shock wave in the numerical design phase. The blast tube was simply a conventional shock tube where the driver section was modified to be linearly diverging in the direction of blast wave travel and linearly converging into a sharp corner in the opposite direction. This modification allowed for reflection of the expansion waves arising from the diaphragm burst. The simplified schematic of the blast tube is shown in Figure 2.5.

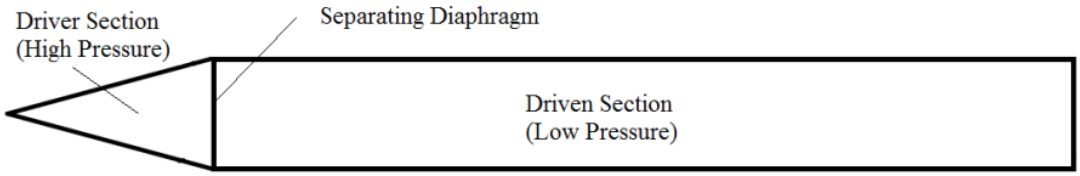


Figure 2.5: simplified blast tube geometry

When the diaphragm bursts, a shock wave travels into the low pressure driven section and an expansion wave travels into the driver section. As the expansion waves travel into the driver section, they reflect off the diverging walls of the driver section back into the low pressure driven section. This starts reducing the properties of air that would have been raised by the leading shock wave. The linear diverging driver section also causes expansion wave focusing as the expansion wave continues traversing into the driver section. At the corner of the driver section the expansion focusing is so intense that it causes extreme reduction in air properties which causes a shock wave to form as a result of the discontinuity that occurs in the air properties. This is how the secondary shock wave forms in the blast tube.

However, Demby (2018) could not detect this secondary shock wave during experimentation. Instead, a reflected blast wave from the closed end of the blast tube was being detected before the secondary shock could reach the pressure transducers.

2.7 Interactions of Shock waves

2.7.1 Diffractions

A normal shock wave is diffracted when it is moving and passes through a sudden area expansion. The most basic type of shock wave diffraction occurs when a shock wave goes over a 90 degree corner. This type of shock wave diffraction is the most useful to this study. This is because many blast wave explosions occur in man-made structures that have 90 degree corners such as buildings (Skews et al. (1967)).

Figure 2.6 shows an incident shock (IS) wave before it is diffracted on a 90 degree corner. As the shock wave is diffracted over the 90 degree corner, shock wave patterns are observed in the perturbed region behind the diffracting shock wave. The patterns are shown in Figure 2.7. These details are provided by Skews et al. (2012) for low incident shock Mach numbers. The flow features are characterised by the incident shock wave (IS) that continues downstream, a curved diffracted shock wave (DS) that propagates down the wall and an expansion wave (EW) that gets reflected back upstream.

The perturbed region is characterised by a vortex (V), shear layer (SL) or slipstream, contact surface (CS), lambda shock (LS) and a viscous vortex (VV) depending on the strength of the incident shock wave. The slipstream forms because of the flow's inability to propagate around a sharp corner. The slipstream forms to enable high-speed flow to interact with stationary flow. The thickness of the slipstream increases as it goes further out from the 90 degree corner. The slipstream curves when it wraps around the vortex. The angle between the top surface of the test piece and the slipstream is called the slipstream angle. The slipstream angle increases with increasing Mach number.

In Figure 2.7 the contact surface emanates from the point where the curved diffracted wave meets the incident shock wave and the reflected expansion wave. The contact surface is observed more clearly in high Mach number flows that create large entropy gradients. The contact surface is less pronounced in weak shock waves with Mach numbers less than 1.07. Figure 2.7 shows that the expansion wave has a circular shape.

The secondary shock wave is formed for Mach numbers greater than 1.6. As the Mach number increases, the secondary shock wave interacts with the vortex to form the terminator.

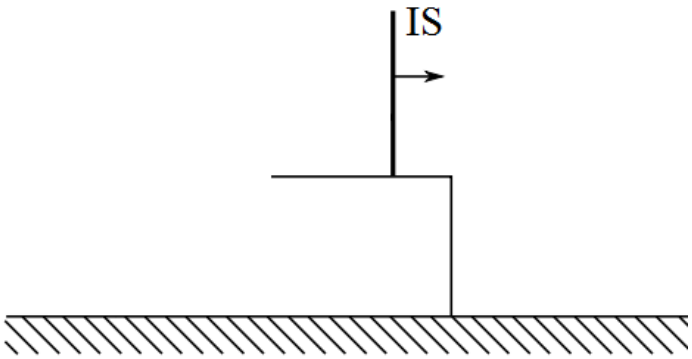


Figure 2.6: Incident shock wave moving towards a 90 degree corner.

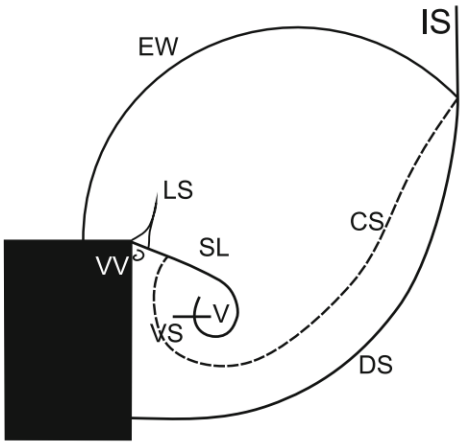


Figure 2.7: Perturbed region behind a low Mach number diffracting shock wave adapted from B. Skews et al. (2012)

.

2.8 Flow visualisation

2.8.1 Shock Waves Visualisation

The methods for shock waves visualisation take advantage of the density discontinuity that the shock wave creates in a fluid. The shadowgraph technique for flow visualisation is one of the simplest techniques for visualising a shock wave. The technique works by using light and the fact that light will be deflected if it encounters a change in density. When light is shone onto a test section where a shock wave is passing on the setup, as seen in Figure 2.8, the light will be deflected through the shock wave because of the change in air density. This will result in spatial variation of the light intensity that will reach the camera. The shock wave will therefore be seen as a shadow by the camera (G. Settles (2002)). Shadowgraphy as

an optical visualisation technique is sensitive to changes of the second derivative of the fluid density (Merzkirch (2012)).

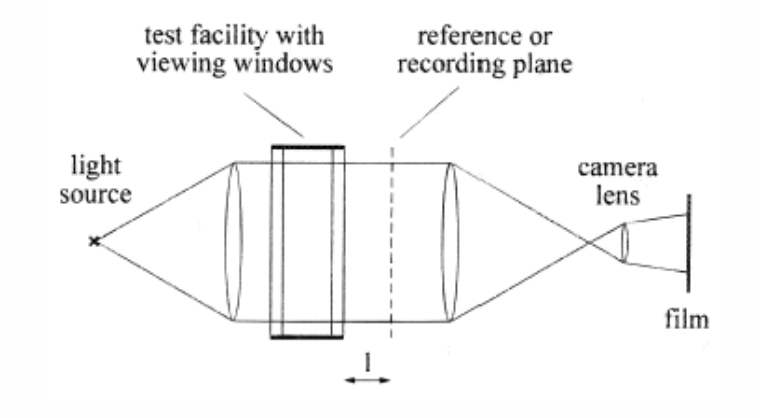


Figure 2.8: The optical setup for the shadowgraphy technique G. Settles (2002)

Schlieren methods work in a similar way to shadowgraphy. They also use the fact that light is deflected when it encounters a change in density in a fluid. The schlieren method setup is shown in Figure 2.9. A bright source of light is passed through a slit such that the light reflected from the mirror will form parallel light rays that will pass through the test section. The light is collected by another concave mirror on the other side of the test section and focused onto a knife edge. In flow of uniform density, the effect of the knife edge is to reduce the image intensity by half. In flow where a shock wave is passing, the light beam is distorted due to the fluid density gradients and it focuses imperfectly. The parts that focus on the area covered by the knife edge are blocked. The positive and negative fluid density gradients in the direction perpendicular to the knife edge will be seen as bright and dark patches on the camera (G. Settles (2002)). The schlieren methods are sensitive to the changes of the first derivative of fluid density while shadowgraphy techniques depend on the changes of the second derivative of the fluid density (Merzkirch (2012)).

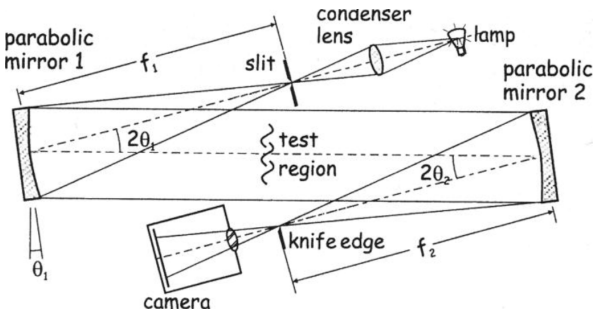


Figure 2.9: The optical setup for the schlieren flow visualisation technique adapted from G. S. Settles and Hargather (2017)

2.9 Shock Wave strength

The strength of a shock wave is given by the energy that the shock wave carries and increases with the Mach number of the shock wave, M (Anderson (1990)). The Mach number of a shock wave is given by

$$M = \frac{v}{c} \tag{2.6}$$

where;
v is the velocity of the shock wave and
c is the speed of sound in the medium in which the shock wave is propagating.

For a shock wave propagating in an ideal gas the speed of sound is given by

$$c = \sqrt{\gamma RT} \tag{2.7}$$

where;
γ is the ratio of specific heat, which is 1.4 for air,
R is the universal gas constant which is approximately $287.1 m^2 s^2 K^{-1}$ and
T is the absolute temperature in Kelvin, K.

Chapter 3 Research objectives

The purpose of this research is to:

1. Generate blast waves with good visual quality and good Friedlander pressure decay profiles using non-explosive methods.
2. Study the diffraction of blast waves around a 90 degree corner using schlieren methods for flow visualisation.
3. Study the perturbed region behind a blast wave diffracting around a 90° corner.
4. Establish the behaviour of expansion waves in the diffraction of blast waves.

Chapter 4 Research apparatus

4.1 Experimental apparatus

4.1.1 Blast tube

The blast tube used for experiments was designed by Demby (2018). This is shown in Figure 4.1. The blast tube consisted of the pressure vessel, the driver section, the driven section and the test section.

The pressure vessel:

The pressure vessel that was used was manufactured by Arlec Engineering Works. It was certified to be pressurised to 40bar. The pressure vessel had an internal diameter of 150mm and a length of 600mm. The pressure vessel was used to pressurise the driver section to the initial pressure. The driver section was encased inside the pressure vessel. This allowed the experiments to be conducted without certifying the driver section.

The driver section:

The driver consisted of a 30 degree linearly diverging section. The open end of the driver section had internal dimensions of 76mm x 76mm. The side view of the internal section of the driver section is shown in Figure 4.3. The driver section was placed inside the pressure vessel and loaded directly from the pressure supply. This solved the problem of the poppet valve opening during tests that was encountered by Demby.

The driven section:

The driven section had an overall length of 3480mm. It was constructed from square tubes with internal dimensions of 76mm x 76mm. PCB pressure transducers were connected at 2980 mm and 3230 mm from the diaphragm. The calibration data for the transducers is

given in Table 4.1. The transducers that were used had model and serial numbers 113B21 S/N20595 on channel one and 113A21 S/N14051 on channel two.

Table 4.1: Calibration data for the pressure transducers that were used in the experiment

Model	**Serial Number**	**Calibration** [mV/PSI]
113B21	20595	24.75
113A21	14051	24.92

Test Section and Test Pieces:

The test section was 76 mm wide, with a height of 232 mm and a length of 295 mm. It had two doors with circular glass windows of diameter 235 mm. This allowed schlieren photographs to be taken. A 90 degree test piece made from mild steel was used.

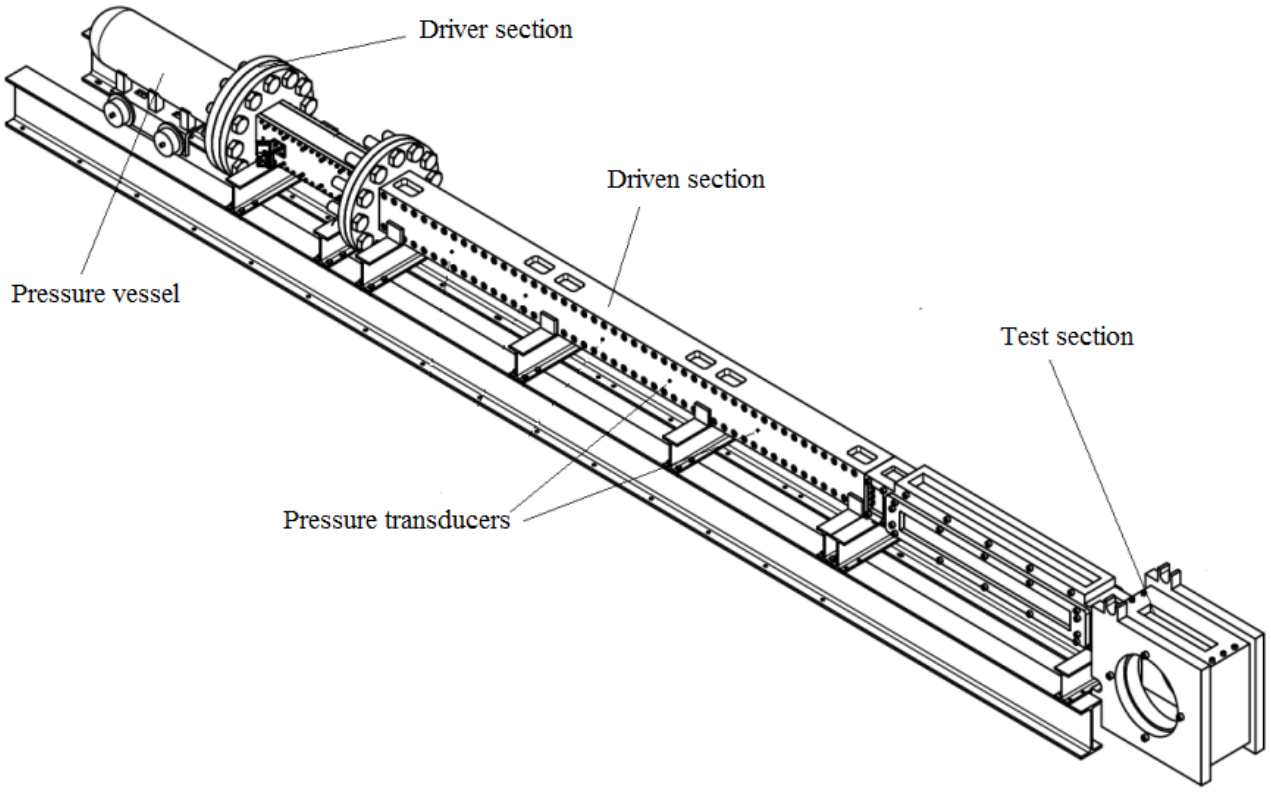


Figure 4.1: Schematic of the blast tube

4.1.2 Schlieren setup

Schlieren flow visualisation techniques were used to visualise blast waves as they diffracted around the 90 degree corner. The schlieren optical setup that was used for the experiment is shown in Figure 4.2. It consists of a high intensity light source. A Megaray MR2000LAB was used for this purpose. The light produced by the light source was focused onto a 0.5mm pinhole by a converging lense. The light from the pinhole was then reflected off a parabolic mirror as parallel light rays and directed to pass through the test section. The light was collected by another parabolic mirror at the opposite side of the test section and directed towards a vertical knife edge. A vertical knife edge on a schlieren system ensures sensitivity in the horizontal direction. The light from the knife edge then passed through a converging lense that directed it towards the high-speed camera. A Photron Fastcam SA5 was used for this purpose. The high-speed camera was set to capture 65000 frames per second. This was done to ensure that the development of the flow features behind the leading shock wave were fully captured.

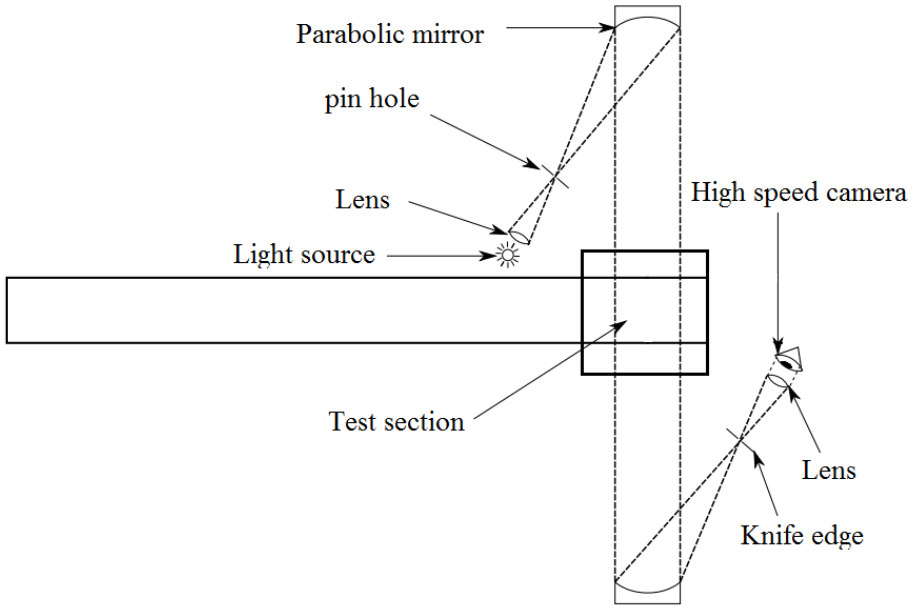


Figure 4.2: Schlieren setup used in the experiment

4.2 Numerical study

4.2.1 Geometry

The geometry of the blast tube was sketched using SolidWorks 2018. The geometry was modelled as a 2-dimensional sketch of the inner dimensions of the blast tube.

The entire blast tube internal was modelled as a single fluid domain. All the edges of the blast tube were modelled as walls. This was done to accurately simulate the actual blast tube since it had steel bounds on all its edges.

Figure 4.3 shows the 2d sketch of the driver section drawn in SolidWorks. The driver section of the blast tube was linearly diverging in the direction of travel of the blast wave and linearly converging into a sharp corner in the opposite direction. This geometry was converted to a step file and imported to Anysys Designer Modeller.



Figure 4.3: Driver section of the blast tube modelled in SolidWorks

The imported geometry is shown in Figure 4.4. This geometry was meshed in Anysys fluent.

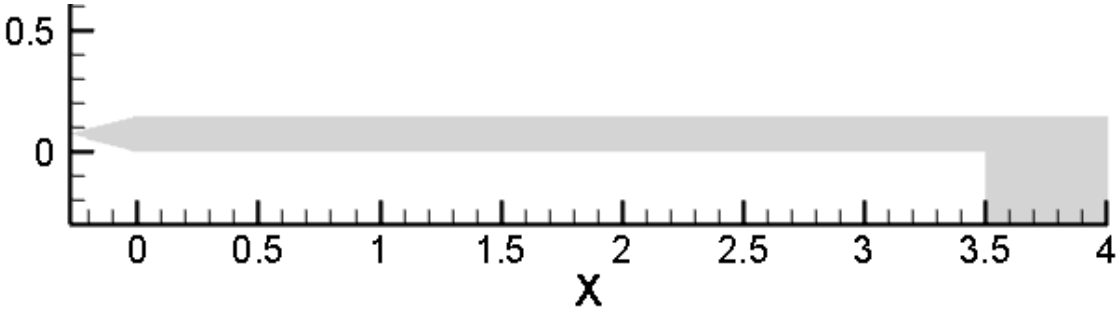


Figure 4.4: Imported blast tube geometry shown in Tecplot

4.2.2 Meshing

The blast tube was modelled as a single fluid domain with wall boundaries. Inflation layers were added on the walls to allow for the accurate modelling of the boundary layer. Figure 4.5 through to Figure 4.8 show the mesh settings that were applied. Figure 4.9 shows the meshed driver section.

Details of "Mesh"

Display	
Display Style	Body Color
Defaults	
Physics Preference	CFD
Solver Preference	Fluent
Relevance	0
Export Format	Standard
Shape Checking	CFD
Target Skewness	Program Controll...
Element Midside Nodes	Dropped
Sizing	
Size Function	Proximity
Relevance Center	Coarse
Initial Size Seed	Active Assembly
Smoothing	Medium
Span Angle Center	Fine

Figure 4.5: The mesh settings for the CFD model

Sizing	
Size Function	Proximity
Relevance Center	Coarse
Initial Size Seed	Active Assembly
Smoothing	Medium
Span Angle Center	Fine
Num Cells Across Gap	Default (3)
Proximity Size Function Sources	Faces and Edges
Proximity Min Size	Default (1.4991e-003 m)
Max Face Size	8.e-003 m
Growth Rate	Default (1.20)
Automatic Mesh Based Defeaturing	Off
Minimum Edge Length	1.e-003 m
Inflation	
Use Automatic Inflation	None

Figure 4.6: The mesh settings for the CFD model

Inflation	
Use Automatic Inflation	None
Inflation Option	Smooth Transition
Transition Ratio	0.272
Maximum Layers	10
Growth Rate	1.2
Inflation Algorithm	Pre
View Advanced Options	No
Assembly Meshing	
Method	None
Advanced	
Number of CPUs for Parallel Part ...	Program Controlled
Straight Sided Elements	
Number of Retries	0
Rigid Body Behavior	Dimensionally Reduced

Figure 4.7: The mesh settings for the CFD model

4.2.3 Solver settings

Ansys Fluent was used for solving the meshed model. The following settings were applied to the solver.

General:

- Solver Type: Density Based

Details of "Mesh"	
Advanced	
Number of CPUs for Parallel Part ...	Program Controlled
Straight Sided Elements	
Number of Retries	0
Rigid Body Behavior	Dimensionally Reduced
Mesh Morphing	Disabled
Triangle Surface Mesher	Program Controlled
Topology Checking	Yes
Use Sheet Thickness for Pinch	No
Pinch Tolerance	Default (1.3492e-003 m)
Generate Pinch on Refresh	No
Sheet Loop Removal	No
Statistics	
Nodes	22931
Elements	22253
Mesh Metric	None

Figure 4.8: The mesh settings for the CFD model

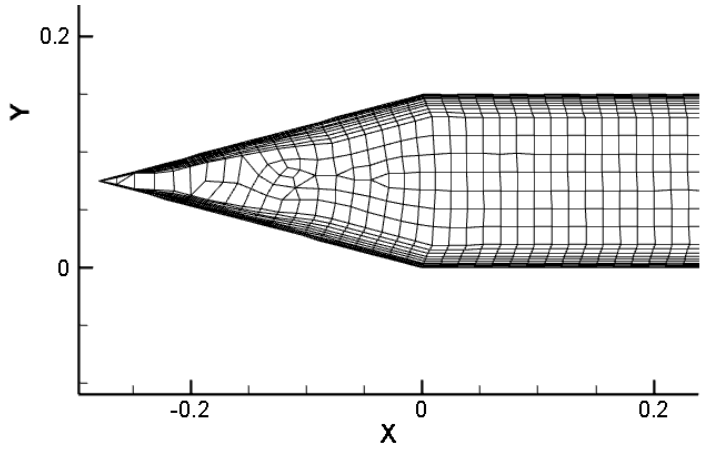


Figure 4.9: The meshed driver section

- Velocity Formulation: Absolute
- Time: Transient Unsteady
- 2D Space: Planar

Models:

- Energy Model: On
- Viscous Model: Realizable k-epsilon, Standard Wall Function

Materials:

- Fluid: Air (Ideal gas model)

Cell Zone Conditions:

- Operating Conditions: Operating Pressure = 0Pa

Boundary Conditions: All boundaries were modelled as walls.

Soving settings Solution Methods:

- Formulation: Implicit
- Flux Type: Roe-FDS
- Spatial Discretization:
  - Gradient: Least Square Cell Based
  - Flow: Second Order Upwind
- Transient Formulation: First Order Implicit

Solution Controls:

- Courant Number: 0.5

Residual Convergence Monitors:

- Continuity Absolute Criteria = 1×10^{-4}
- x-Velocity Absolute Criteria = 1×10^{-4}
- y-Velocity Absolute Criteria = 1×10^{-4}

- Energy Absolute Criteria = 1×10^{-6}
- k Absolute Criteria = 1×10^{-5}
- Epsilon Absolute Criteria = 1×10^{-5}

Solution Initialization:

- Initialization Method: Hybrid Initialization. The driver section was patched to the required driver pressure of 600kPa.
- Reference Frame: Absolute
- Initial Pressure: 101325Pa
- Initial Temperature: 300K

Chapter 5 Methodology

5.1 Experimental

5.1.1 Compressed air storage

The compressed air that was used to pressurise the driver section of the blast tube was obtained from a pressure vessel in the Northwest Engineering laboratory. The pressure vessel was pressurised to between 11 bar and 14 bar before each experimentation session commenced. The following procedure was followed to pressurise the pressure vessel:

1. Check that the air dryer unit is switched off.
2. Close the air dryer bleed valves by first closing the receiver tank valve and then the heater valve.
3. Turn on the solenoid for the pressure vent system.
4. Turn on the water sump supply valve.
5. Open the cooling water valve.
6. Turn on the air compressor.

The compressor that was used to pressurise the pressure vessels turns off automatically when the maximum storage pressure of 14 bar is reached. This ensures that the safe operating pressure of the pressure vessel is not exceeded. The pressurisation system was turned off before commencement of testing. The procedure to turn off the pressurisation system is as follows:

1. Turn off the air compressor.
2. Close the cooling water supply valve.

3. Turn off the water supply pump.
4. Turn off the solenoid for the pressure venting system.
5. Bleed the air dryer unit by slowly opening the receiver tank valve and vent the air until the pressure gauge attached to the unit reads 0 $lbin^{-2}$
6. Open the heater valve.

5.1.2 Pre-Testing Procedure

The following procedure was followed at the beginning of every testing session:

1. Switch on laptops being used to record diffraction images and pressure data.
2. Switch on all instrumentation: signal conditioner, oscilloscope and delay box.
3. Set the Volt/Division and Time/Division of the oscilloscope to the correct values for the planned experimentation.
4. Check that the pressure transducers have been connected correctly and are responsive to pressure changes.
5. Switch on the high-speed camera and light source.
6. Remove the covers of the parabolic mirrors.

5.1.3 Blast Tube Testing Procedure

The following procedure was followed for every test run:

1. Use a template to cut out a diaphragm.
2. Place a new diaphragm on the driver section flange and tape it in place.
3. Roll the driver section back into place and make sure the diaphragm material is held tightly against the flange of the driven section.
4. Bolt the driver section, pressure vessel and driven section flanges together.
5. Inspect the blast tube to make sure that all components and pipes are bolted and attached securely.
6. Close the door to the the blast tube laboratory room.

7. Set the delay of the trigger box to the required value for the experiment being run..
8. Arm the trigger box of the oscilloscope and the high-speed camera.
9. Ensure that all the valves on the control panel are closed.
10. Open the valve on the high pressure line supplying compressed air from the lab pressure vessel.
11. Open the safety valve on the control panel.
12. Slowly open the pressure supply valve on the control panel to pressurise the driver section.
13. Note the pressure displayed on the pressure gauge when the diaphragm bursts and close the supply valve on the control panel immediately.
14. Close the supply valve on the high pressure line.
15. Open the release valve on the control panel to vent the compressed air remaining in the pressure vessel.
16. Close the release valve and safety valve on the control panel.
17. Note the difference in time between the recording of the shock front at the first pressure transducer and the recording of the shock front at the second pressure transducer, δt , in order to determine the Mach number of the generated blast wave.
18. Record the burst pressure, room temperature and atmospheric pressure.
19. Save and store the oscilloscope pressure readings as well as the photographs and videos taken by the high-speed camera.

5.1.4 Blast Tube Shut Down Procedure

The following procedure was followed at the end of each testing session:

1. Detach the driver section and pressure vessel from the driven section by loosening and removing the bolts attaching the two sections.
2. Roll the driver section away from the driven section.
3. Remove the burst diaphragm from between the driver section flange and the driven section flange.

4. Open the doors of the test section and insert the high pressure hose into the tube opening at the driven section flange to blow out any diaphragm fragments stuck in blast tube.

5. Ensure that all the valves on the control panel as well as the supply valve on the high pressure line are closed.

6. Turn off the high-speed camera and light source.

7. Replace the parabolic mirror covers back onto the mirrors.

8. Turn off all instrumentation: signal conditioner, oscilloscope and delay box.

9. Turn off laptops being used to record photographic and pressure data.

10. Open the test section doors.

5.1.5 Precautions

The following safety precautions were observed during the experimentation:

1. Hearing protection must be worn while bleeding the air dryer unit and during the testing procedure.

2. The driven and test sections of the blast tube must be inspected for any diaphragm debris before closing up and running a test.

3. Ensure that the optical equipment is not accidentally moved or bumped into.

4. Ensure that the optical mirrors and glass test section windows are not scratched or otherwise damaged.

5. The glass test section windows as well as the parabolic mirrors should be cleaned with a soft cloth and acetone between tests to ensure that clear images are captured.

6. When changing the driver section and driven section inserts as well as the test pieces, make sure to inspect and tighten the bolts to ensure that the the inserts and pieces are securely fixed in place.

7. Blow the warning whistle before testing so as to alert other laboratory workers of the imminent loud blast so that they protect their ears.

5.2 Flow Visualisation

The images of blast wave diffraction around a 90 degree corner were captured using schlieren flow visualisation techniques. The optical set-up used was the standard z-configuration as shown in Figure 4.2. Two rails on either side of the test section were used to support the light source, lens and pinhole on one side and the knife edge, lens and high-speed camera on the other side. Both rails were placed at angles of approximately 10 degrees to the perpendicular axis of the tube through the test section. Parabolic mirrors with a diameter of 317.7mm and focal lengths of 1905mm were used on either side of the test section. Initially the light source was replaced with a bright laser light which was used for perfectly aligning all the components of the z-configuration. Great care and effort was taken to ensure that the light reflecting off the parabolic mirror entered the test section perpendicular to the test section. Any slight misalignment would result in poor image quality. A Xenon lamp and a Megaray MR2000LAB were used as the light source. The light from the lamp was converged to a pinhole by a converging lens. The pinhole was placed on the rail such that its distance to the the parabolic mirror was equal to the focal length of the parabolic mirror. The light from the pinhole shone onto the parabolic mirror and reflected off to pass through the test section as paralleled light. The light was collected by the parabolic mirror on the other side of the test section and reflected to focus on the vertical knife-edge. The vertical knife-edge was placed on the rail such that its distance to the parabolic mirror was equal to the focal length of the parabolic mirror. The light from the knife edge was collected by a lens which directed it into the sensor of the high-speed camera. The high-speed camera that was used is a Photron Fastcam SA5. It was set to capture 65000 frames per second.

Chapter 6 Observations

This section contains unprocessed data collected from the experimental procedures followed in chapter 5.

6.1 Experimental data

Table 6.1 shows the data for each test during the experiments. The diaphragm material was chosen from 3 different types of polyester film thicknesses. Different number combinations of each type of the polyester films were used to create different strengths of the blast waves. The time for the leading shock wave to travel between the two pressure transducers, air temperature and atmospheric pressure during each test were recorded and shown in Table 6.1. The time for the leading shock wave to travel between the pressure transducers was measured by determining the time between the peaks in Figure 6.1.

Table 6.1: Experimental data

Test	Diaphragm			T [$°C$]	P_{atm} [mbar]	time [μs]
	$25\mu m$	$50\mu m$	$100\mu m$			
1	0	0	1	23	830.0	665
2	1	0	0	22	836.4	782
3	0	1	0	22	836.6	723
4	1	1	0	22	836.6	684
5	1	0	1	22	836.6	645
6	0	1	1	23	836.6	606
7	0	0	2	23	836.4	600
8	1	0	0	22.5	836.4	782
9	0	1	0	22.5	836.6	743
10	1	1	0	22.5	836.6	704
11	0	0	1	22	830.0	665
12	1	0	1	22	830.0	645
13	0	1	1	22	834.0	606
14	0	0	2	22	834.0	600

Table 6.2: Pressure transducer peak voltages

Test	P_{atm} [mbar]	V_{ch1} [V]	V_{ch2} [V]
1	830	0.263529	0.370196
2	836.4	0.081569	0.207059
3	836.6	0.156863	0.269804
4	836.6	0.225882	0.338824
5	836.6	0.351373	0.451765
6	836.6	0.357647	0.458039
7	836.4	0.326275	0.432941
8	836.4	0.075294	0.200784
9	836.6	0.144314	0.263529
10	836.6	0.213333	0.332549
11	830	0.263529	0.370196
12	830	0.294902	0.401569
13	834	0.294902	0.407843
14	834	0.332549	0.439216

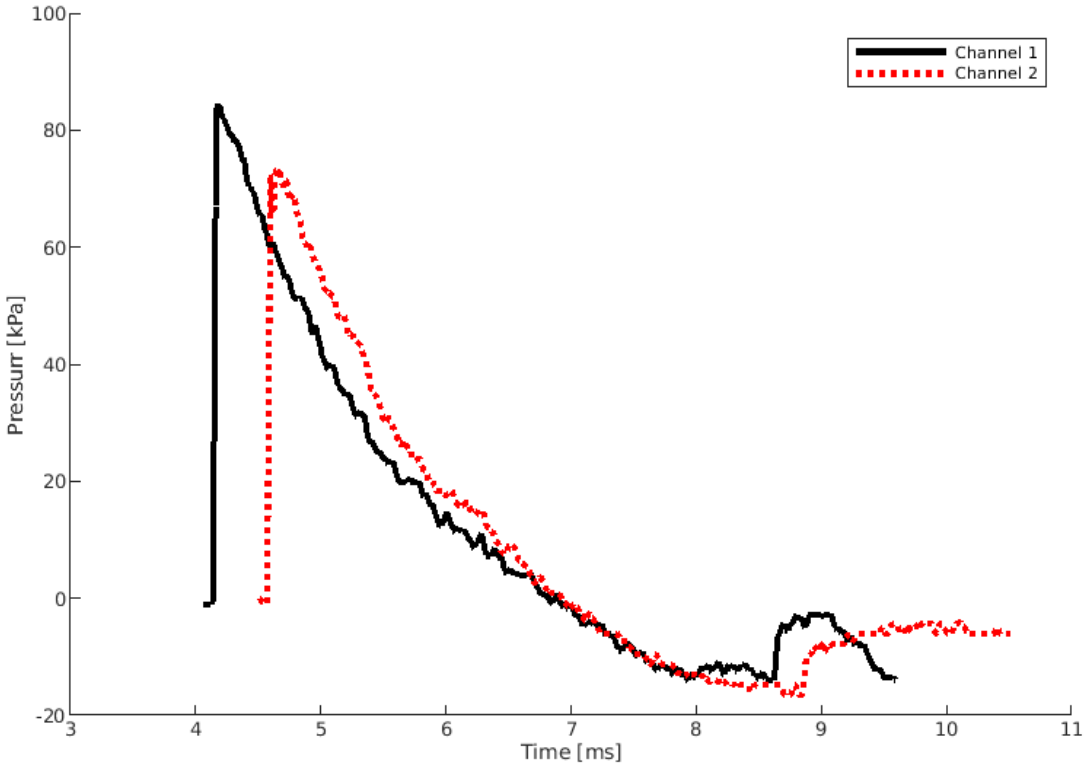


Figure 6.1: Unprocessed oscilloscope pressure trace

Chapter 7 Data Processing

This section describes the steps that were taken in processing the experimental and numerical data presented in chapter 6.

7.1 Mach Number Calculation

With the distance between the pressure transducers known, d_t and the time for the shock wave to move between the transducers measured from the oscilloscope, t, the shock wave speed, v was calculated simply as

$$v = \frac{d_t}{t} \tag{7.1}$$

The measured room temperature was converted to Kelvins as

$$T(K) = T(^oC) + 273.14 \tag{7.2}$$

Then the speed of sound, c was calculated from Equation 2.7 as

$$c = \sqrt{\gamma RT}$$

with $\gamma = 1.4$ and $R = 287.1 m^2 s^2 K^{-1}$

With the shock wave velocity, v and the speed of sound in air, c known, the Mach number, M of the shock wave was then calculated from Equation 2.6 as

$$M = \frac{v}{c}$$

The calculations for test 1 from Table 6.1 are as follows;

$$T = 23^oC = 296.14K, \Delta t = 665\mu s, d_t = 30cm$$

The speed of the shock wave is calculated as,

$$v = \frac{30 \times 10^{-2} m}{665 \times 10^{-6} s}$$

$$v = 451.13ms^{-1}$$

The speed of sound in air is calculated as,

$$c = \sqrt{1.4 \times 287.1 \times 296.14}$$

$$c = 345.01ms^{-1}$$

Therefore, the Mach number is,

$$M = \frac{451.13}{345.01} = 1.31$$

This procedure was followed for all the tests. The results are shown in Table 7.1.

Table 7.1: Processed experimental data

Test	T [$°C$]	c [ms^{-1}]	t [μs]	v [ms^{-1}]	M
1	23	345.008	665	451.1278	1.31
2	22	344.425	782	383.6317	1.11
3	22	344.425	723	414.9378	1.20
4	22	344.425	684	438.5965	1.27
5	22	344.425	645	465.1163	1.35
6	23	345.008	606	495.0495	1.37
7	23	345.008	600	500	1.44
8	22.5	344.7166	782	383.6317	1.11
9	22.5	344.7166	743	403.7685	1.17
10	22.5	344.7166	704	426.1364	1.24
11	22	344.425	665	451.1278	1.31
12	22	344.425	645	465.1163	1.35
13	22	344.425	606	495.0495	1.34
14	22	344.425	600	500	1.37

7.2 Pressure traces

The data obtained from the pressure transducers was processed in MATLAB. The MATLAB codes used in processing the data are provided in Appendix B. The voltage values were converted to kPa using the calibration factors for the pressure transducers that were provided. The calibration factors for the pressure transducers on each channel are shown in Table 4.1

The peak voltages shown in Table 6.2 were converted kPa using the calibration factors given in Table 4.1.

The conversion for the peak voltage on test 1 channel 1 from Table 6.2 is as follows:

$$P_{peak} = \frac{263.529}{24.75} \times 6.89476$$

$$P_{peak} = 73.41kPa$$

The peak pressures for the rest of the tests are shown in Table 7.2. The peak pressures during the experiments were all less than 1 bar. Therefore, Equation 2.1 was used to model the theoretical blast wave decay profile.

Table 7.2: Pressure transducer peak pressures

Test	$P_{atm}[mbar]$	$P_{ch1}[kPa]$	$P_{ch2}[kPa]$
1	830	73.41	71.06
2	836.4	22.72	20.13
3	836.6	43.70	41.42
4	836.6	62.93	59.87
5	836.6	97.89	94.79
6	836.6	99.63	96.67
7	836.4	90.89	88.12
8	836.4	20.98	18.50
9	836.6	40.20	37.93
10	836.6	59.43	56.53
11	830	73.41	71.08
12	830	82.15	79.64
13	834	82.15	79.65
14	834	92.64	90.32

The pressure decay profiles were normalised by dividing all the pressure values by the peak pressure. This was done for easier comparison of the pressure decay profiles. The results for this are shown in Figure 8.1, Figure 8.12, Figure 8.13 and Figure 8.17.

7.3 Positive Impulse

The impulse was calculated based on Equation 2.4. This was done by calculating the area under the graph in the positive phase. This was done using the trapz() function in MATLAB from a time of $4.4ms$ to $7ms$. The obtained results are shown on Figure 8.15.

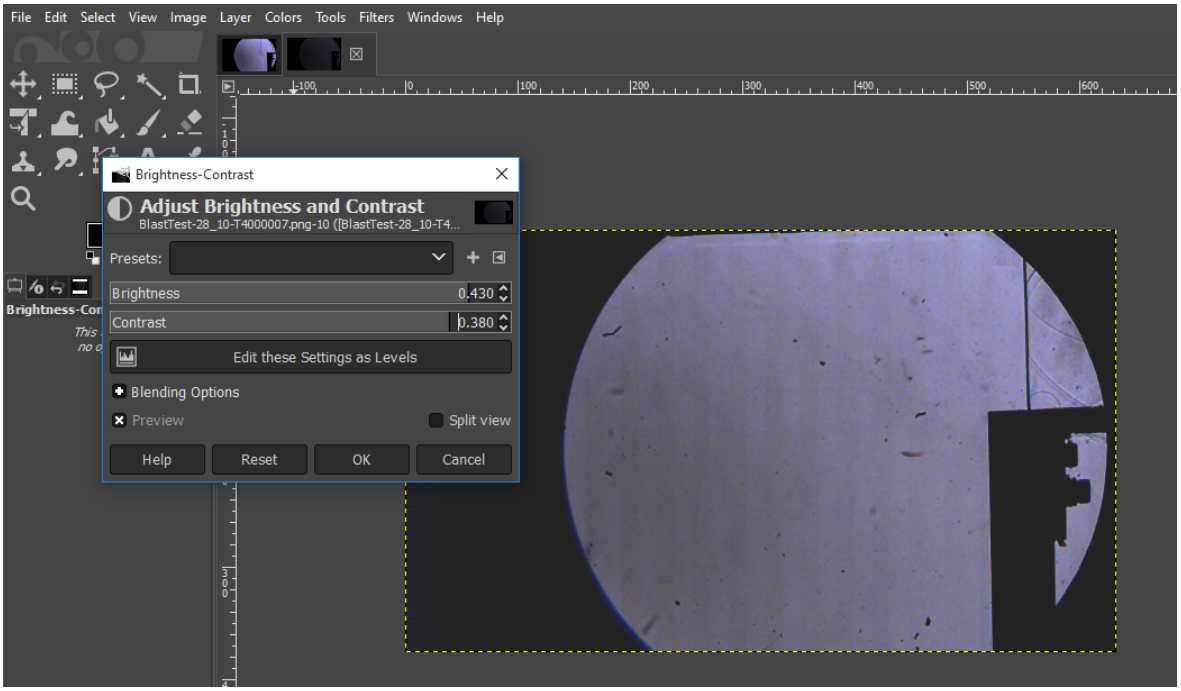


Figure 7.1: Image after processing

7.4 Image Processing

The schlieren images obtained from the high-speed camera were processed using GIMP photo editing software to enhance the image quality. Figure 7.1 shows the image enhancement using the software. The images were resized to ensure that the aspect ratio matched with the CAD drawings of the test section.

Chapter 8 Results and Discussion

8.1 Pressure Traces

8.1.1 Experimental pressure trace vs Friedlander

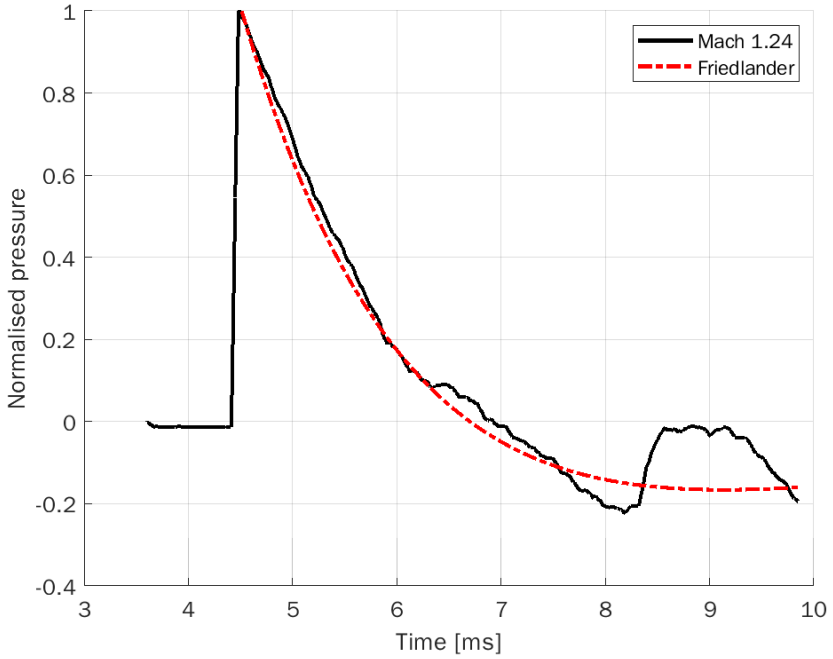


Figure 8.1: Experimental pressure trace vs Friedlander pressure trace

Figure 8.1 shows the experimental pressure decay profile compared to the Friedlander decay profile. Peak over-pressures were normalised to unity for better comparison of the decay profiles. There is strong correlation between the experimental and the analytical decay profiles. However, in the middle of the negative phase there is a discrepancy that occurs.

This discrepancy can be attributed to the formation of the secondary shock wave during the experiment. The Friedlander decay profile does not take into consideration the formation of the secondary shock wave. During the experiment a secondary shock wave is formed when the expansion waves propagating in opposite direction to the blast wave implode at the apex of

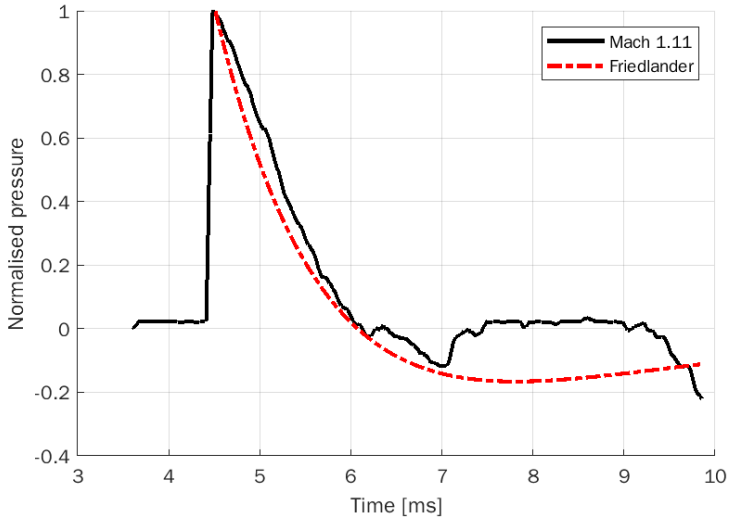


Figure 8.2: Experimental trace vs Friedlander pressure profile at Mach 1.11

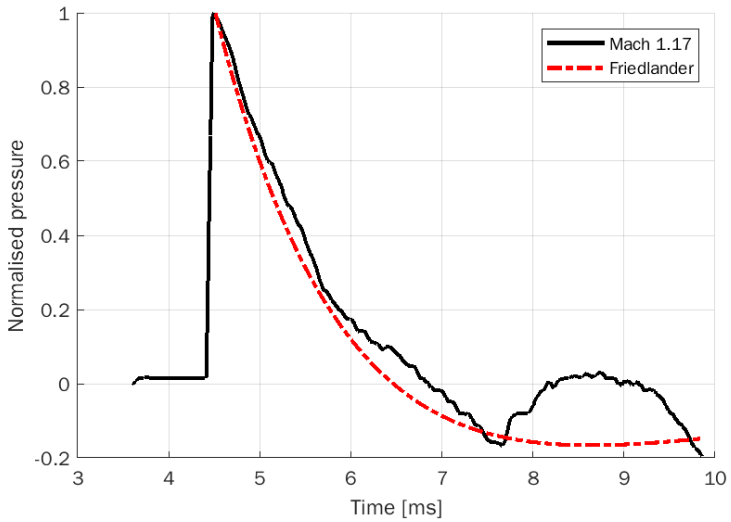


Figure 8.3: Experimental trace vs Friedlander pressure profile at Mach 1.17

the linearly converging walls of the blast tube. This results in a reduction in the air properties of the air behind (density, temperature and pressure). When the expansion waves implode at the center, extremely low temperatures, densities and pressures results in the gas which is then equalised by the formation of a shock wave.

The secondary shock wave can be seen in Figure 8.1 at $\approx 8.4ms$ as a sharp increase in pressure followed by a gradual decrease. It should be noted that the sharp increase in pressure caused by the secondary shock wave stays within the negative phase.

Since there is strong correlation of the experimental decay profile and the Friedlander decay profile in the positive phase, the positive impulse of both decay profiles will be similar. The

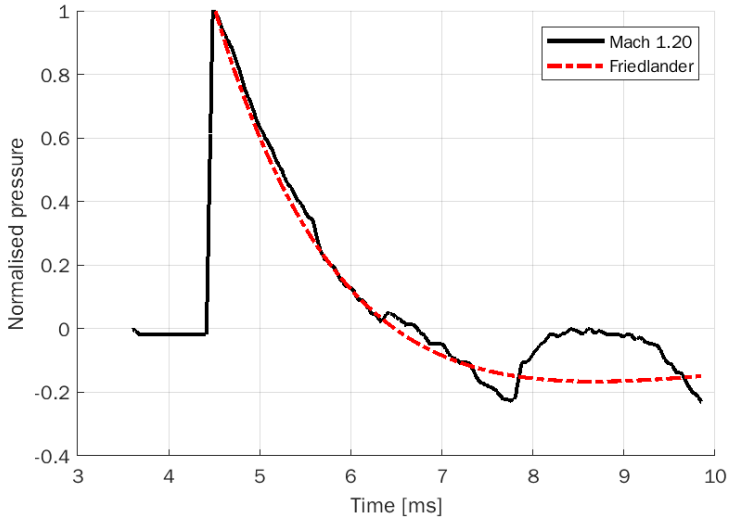


Figure 8.4: Experimental trace vs Friedlander pressure profile at Mach 1.20

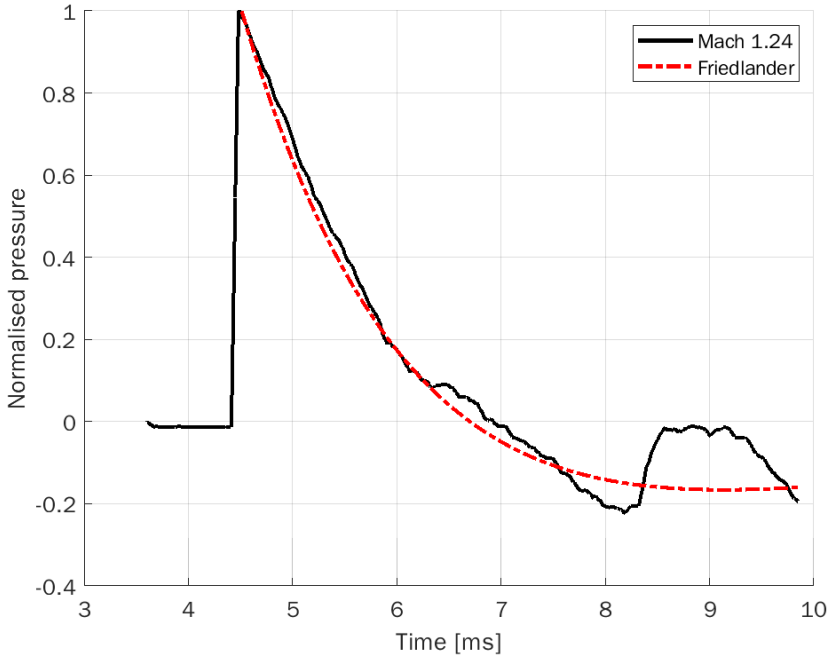


Figure 8.5: Experimental trace vs Friedlander pressure profile at Mach 1.24

blast impulse is calculated using Equation 2.4 or simply as the area under the pressure decay curve in the positive phase. During an explosion the damage is caused by forces created in the positive phase. This means that the blast tube can be used to study and mitigate damage that can happen to various structures during an explosion.

Figure 8.2 through to Figure 8.11 shows the experimental pressure traces compared with the Friedlander pressure profiles from Mach 1.11 to Mach 1.44. For low Mach numbers in Mach 1.11 (Figure 8.2) and Mach 1.17 (Figure 8.3) the experimental pressure decay profiles do not fit the Friedlander profiles very well. However, as the Mach numbers increase in Mach

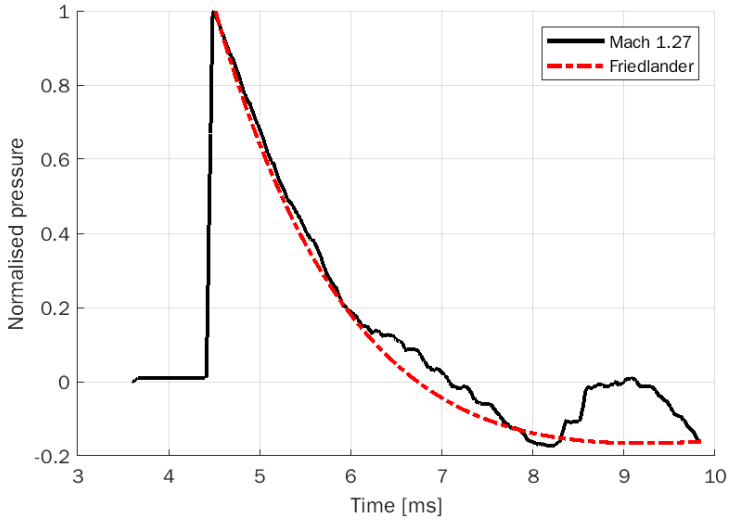


Figure 8.6: Experimental trace vs Friedlander pressure profile at Mach 1.27

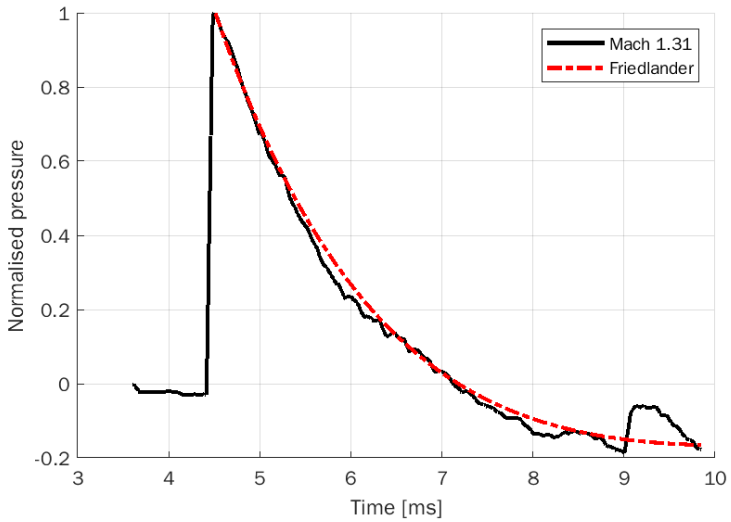


Figure 8.7: Experimental trace vs Friedlander pressure profile at Mach 1.31

1.20 (Figure 8.4), Mach 1.24 (Figure 8.5), Mach 1.27 (Figure 8.6), Mach 1.31 (Figure 8.7), Mach 1.34 (Figure 8.8), Mach 1.35 (Figure 8.9), Mach 1.37 (Figure 8.10) and Mach 1.44 (Figure 8.11) the experimental pressure decay profiles become more exponential and fit the corresponding Friedlander profiles very well. This observation shows that the linearly diverging tube does not produce good blast waves at very low Mach numbers. However, the linearly diverging tube produces good blast waves for Mach numbers greater than 1.20.

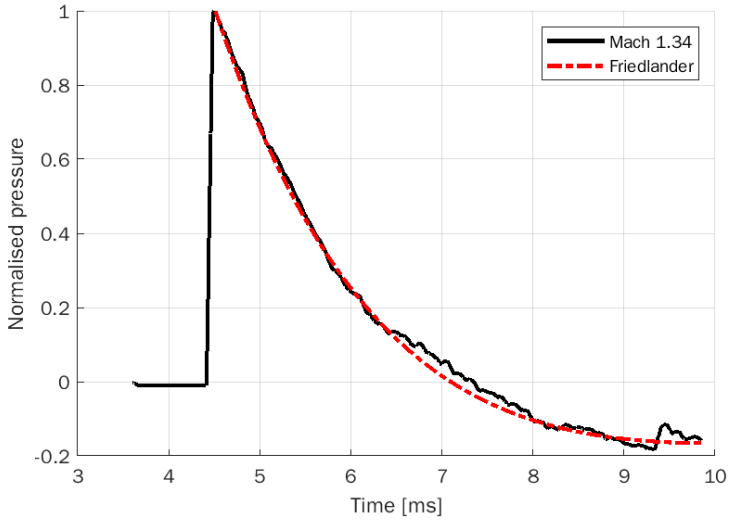


Figure 8.8: Experimental trace vs Friedlander pressure profile at Mach 1.34

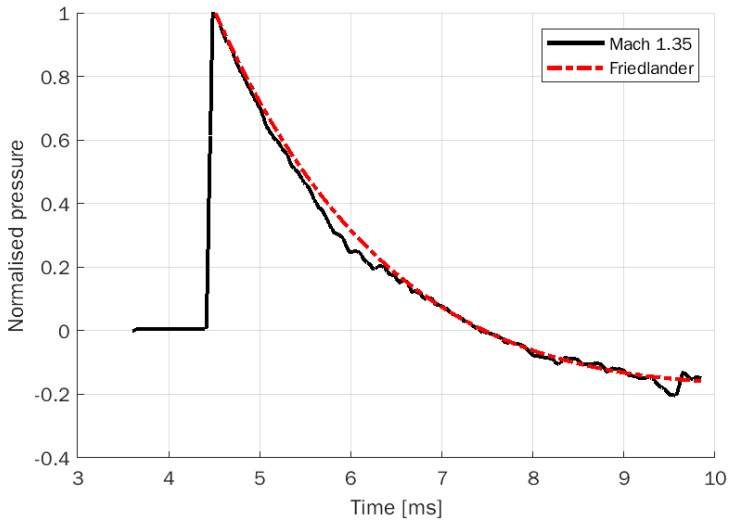


Figure 8.9: Experimental trace vs Friedlander pressure profile at Mach 1.35

8.1.2 Experimental pressure trace vs CFD

Figure 8.12 shows the experimental decay profile compared to the numerical pressure decay profile obtained using CFD Ansys software. The inside dimensions of the blast tube used in the experiment were modelled using Solidworks software and imported to CFD. The two pressure traces in Figure 8.12 show strong conformity in both the positive and the negative phases. Both decay profiles show the formation of the secondary wave at the same time of $\approx 8.4ms$. This validates the properties of the numerical blast wave to be the same as the experimental blast wave. Therefore, further studies into blast waves can be carried out at low costs using the numerical simulations with confidence. This will minimise experimental

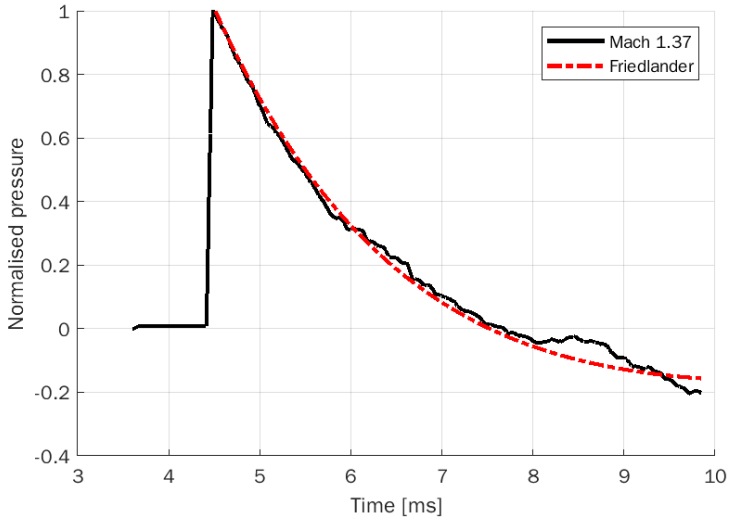


Figure 8.10: Experimental trace vs Friedlander pressure profile at Mach 1.37

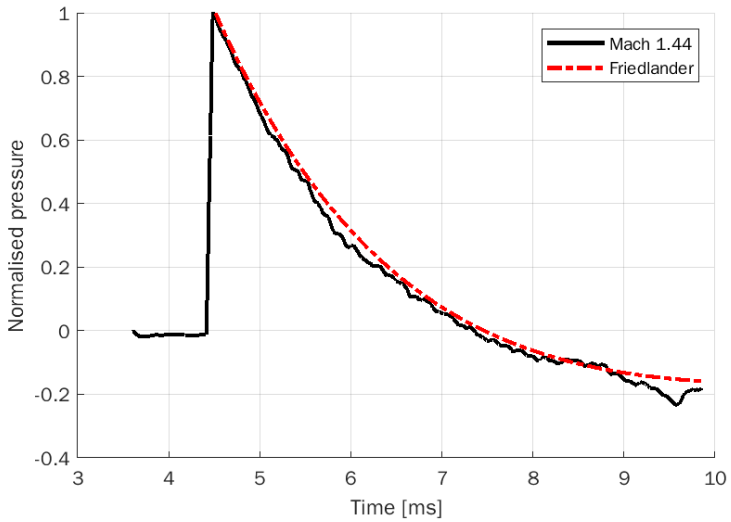


Figure 8.11: Experimental trace vs Friedlander pressure profile at Mach 1.44

costs. These studies can include investigations into impact forces on a structure during an explosion and interactions and propagation of blast waves on various surfaces. This will be useful in mitigating damage caused by explosions on structures.

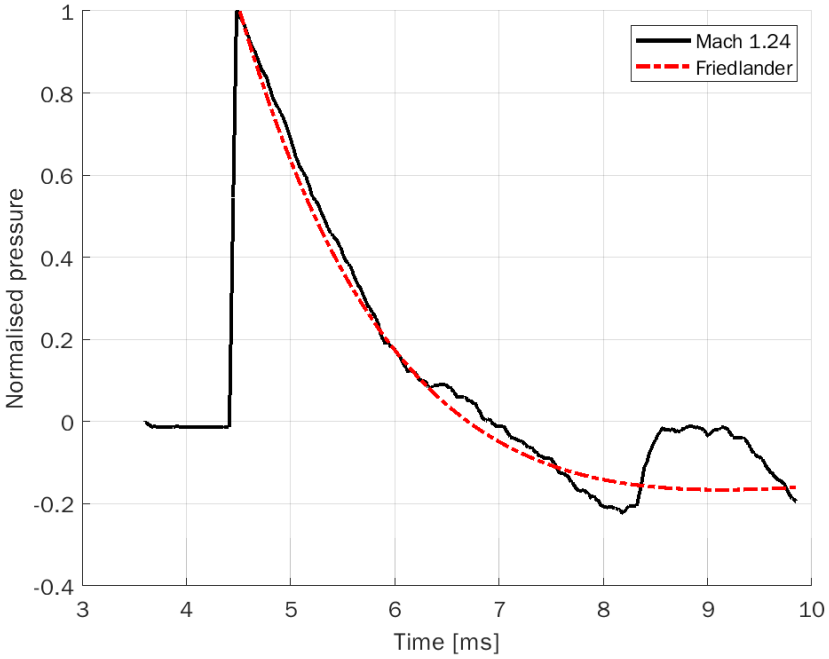


Figure 8.12: Experimental pressure trace vs CFD pressure trace

8.1.3 CFD pressure trace vs Friedlander

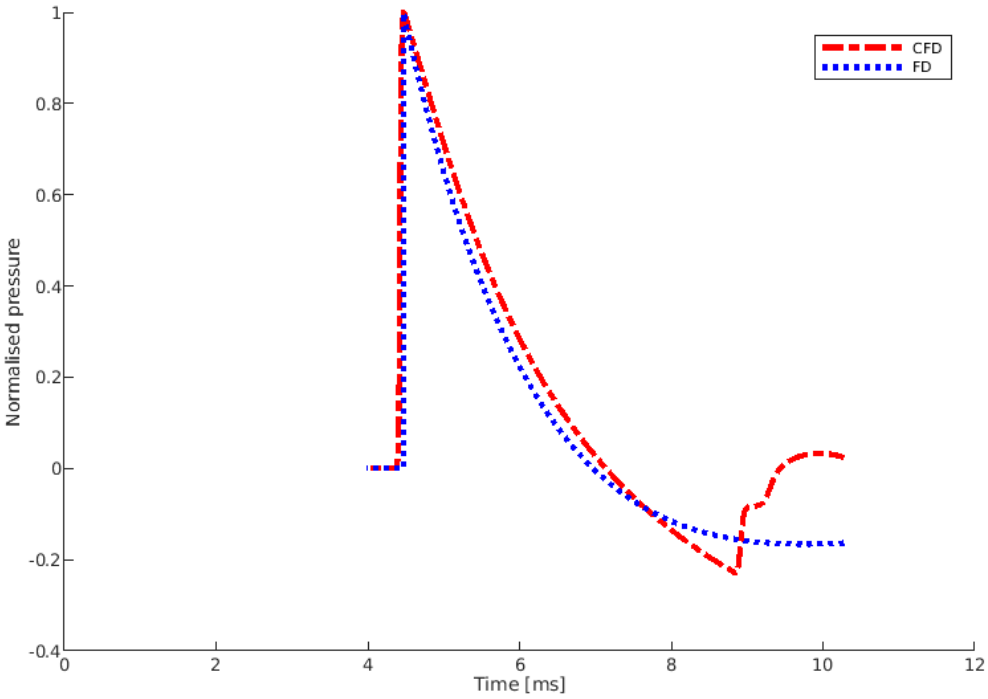


Figure 8.13: Friedlander pressure trace vs CFD pressure trace (Mach 1.24)

Figure 8.13 shows the pressure decay profile obtained in using CFD compared to the Friedlander pressure decay profile. This shows a similar pattern to the one shown in Figure 8.1 for the experimental decay and Friedlander decay. There is strong conformity of the decay profiles in the positive phase. However, in the negative phase there is a discrepancy. This discrepancy is due to the formation of the secondary shock wave in the CFD decay profile. The secondary shock wave can be seen as a sharp increase in pressure at $\approx 8.4ms$. The Friedlander profile does not predict the formation of the secondary shock wave.

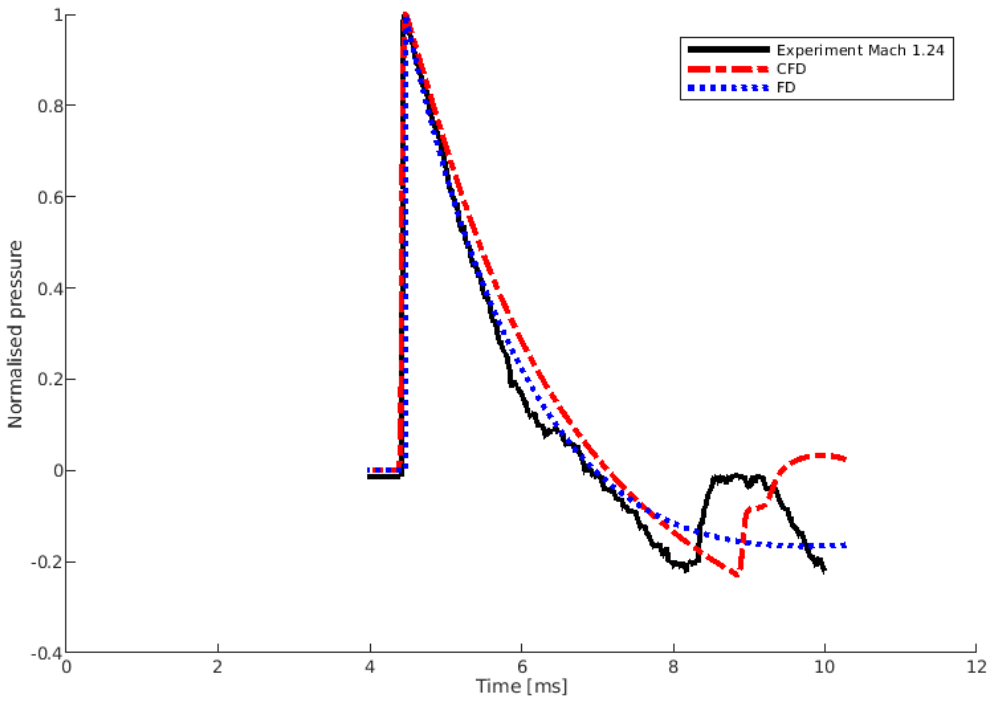


Figure 8.14: Experimental pressure trace vs Friedlander pressure trace vs CFD pressure trace

8.1.4 Positive Impulse

Figure 8.14 shows all three graphs drawn together. All three traces look sufficiently similar. The positive impulse for each graph was calculated for better comparison of the decay profiles.

Figure 8.15 shows the positive impulse that was calculated for the normalised pressure decay profiles. The experimental Impulse differs from the Friedlander impulse by 1.08%. This is a negligible difference. This shows that the blast tube used in the experimentation is able to produce blast waves which create similar loadings on structures to a theoretical blast wave. Therefore, the blast tube can be used to further studies into blast waves with confidence.

The CFD impulse is more than the Friedlander impulse by 2.43%. This implies that the loadings created on structures in CFD will be higher than loads predicted theoretically. The actual positive impulse created by the blast wave during the experiment are also less than the CFD prediction from the impulse values by about 1.32%. These are insignificant differences which shows that there is strong correlation in the pressure decay profiles.

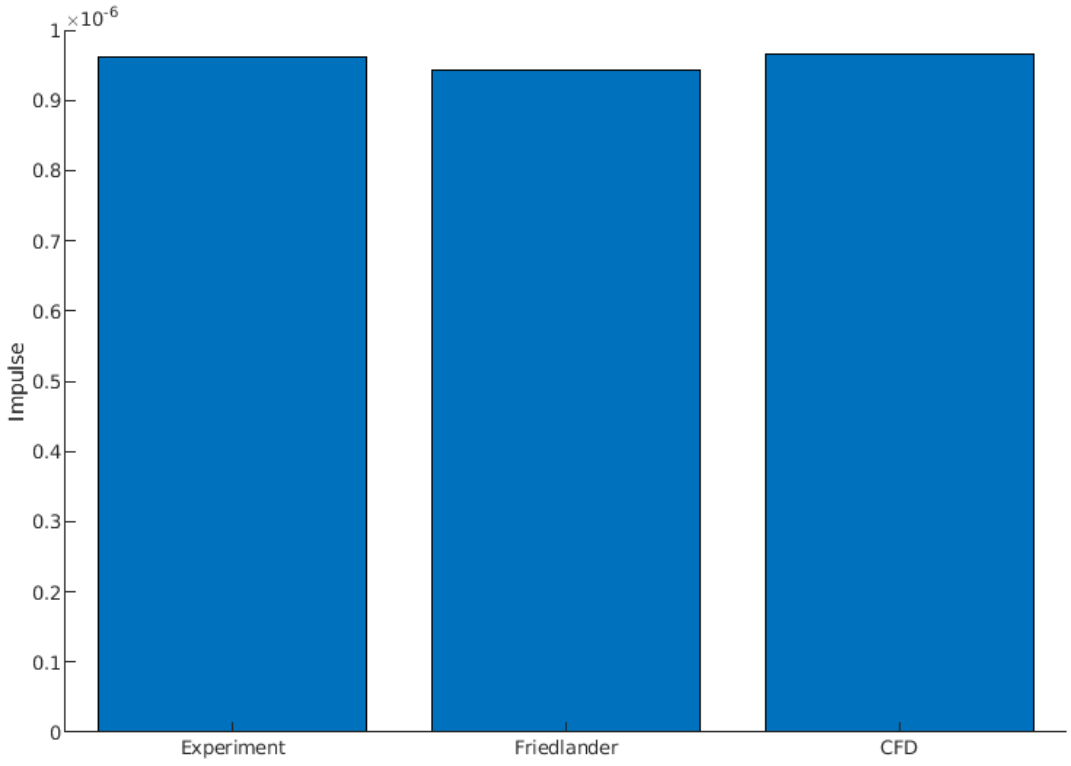


Figure 8.15: Positive impulse calculated from normalised pressure decay profiles (Mach 1.24).

8.1.5 Decay time and second shock time

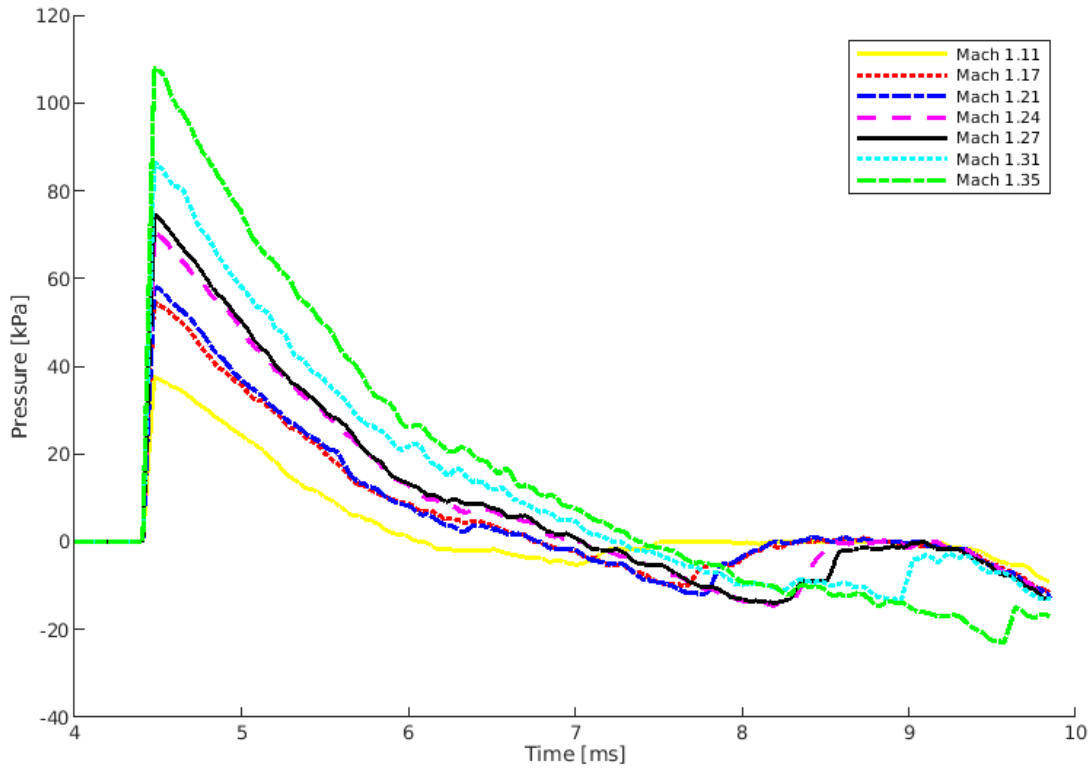


Figure 8.16: Pressure decay profiles for various Mach numbers

Figure 8.16 shows the experimental pressure decay profiles for various Mach numbers. The general decay profile of the blast waves is seen to be similar. It was necessary to normalise the peak overpressure to unity for a better comparison of the blast wave decay profiles. This is shown in Figure 8.17. The decay profiles are following a similar pattern. The decay time or the positive phase duration is increasing as the Mach number increases.

Figure 8.18 shows the variation of the time it takes for the second shock to be detected as the Mach number increases. There is a general increase in the time it takes the second shock wave to be detected as the Mach number increases. The second shock wave is caused by the imploding of the expansion waves on the apex of the linearly diverging driver section. The speed of the second shock is much slower than the speed of the incident shock. This can be seen in Figure 6.1. The time for the leading shock wave to travel between the two transducers is $464.84\mu s$ and the time for the second shock to travel between the two transducers is $697.26\mu s$. This means that speed of the leading shock wave increases faster than the speed of the second shock wave as the Mach number increases. Therefore, as the Mach number increases the leading shock wave and the second shock wave become further apart.

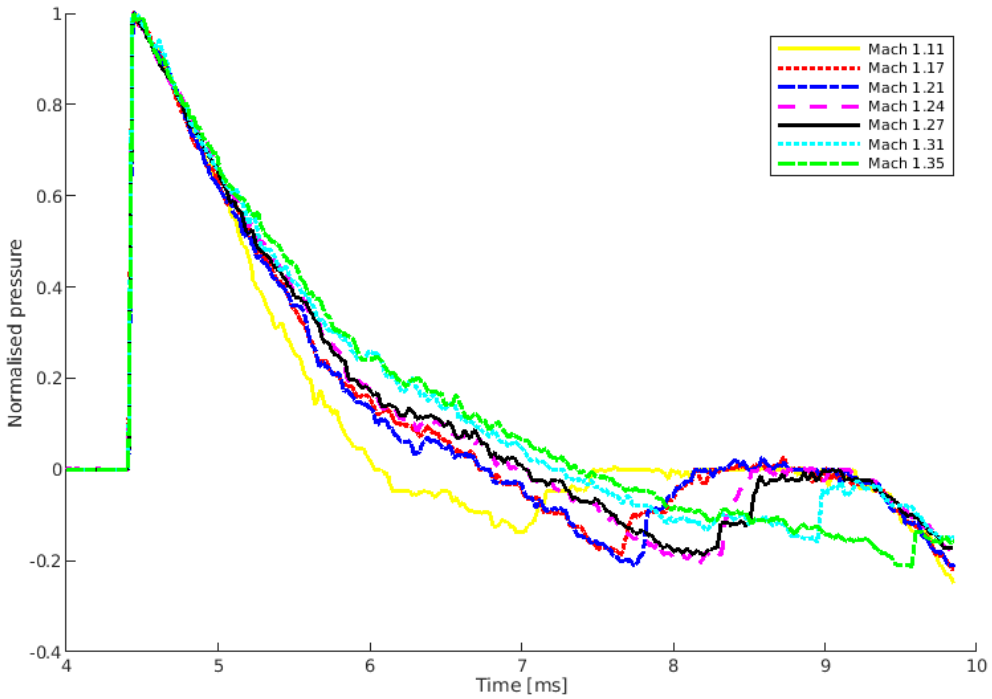


Figure 8.17: Normalised pressure decay profiles for various Mach numbers

8.2 Diffraction

8.2.1 Experimental

Figure 8.19 shows a blast wave diffracting around a 90^o corner. Figure 8.19a shows the incident blast wave just before it starts to diffract. Figure 8.19b and Figure 8.19c shows the development of the blast wave as it starts to diffract around the 90^o corner. The incident blast wave continues downstream while a diffracted blast wave travels down the side of the test piece. A sound wave is also produced when the diffraction starts in Figure 8.19b. The sound wave, which is the leading edge of the reflected expansion from the corner, can be seen travelling back upstream in Figure 8.19c, Figure 8.19d and Figure 8.19e.

Figure 8.19b through to Figure 8.19h show that as the diffraction progresses, the straight leading wave gets smaller while the curved diffracted wave gets bigger.

As soon as the diffraction starts in Figure 8.19b, a vortex forms on the apex of the 90 degree corner. The vortex is seen as a black dot with bright edges in the images Figure 8.19b through to Figure 8.19h. The vortex grows in size and swirls down from the apex of the corner as the diffraction progresses. The vortex is attached to the test piece through a shear

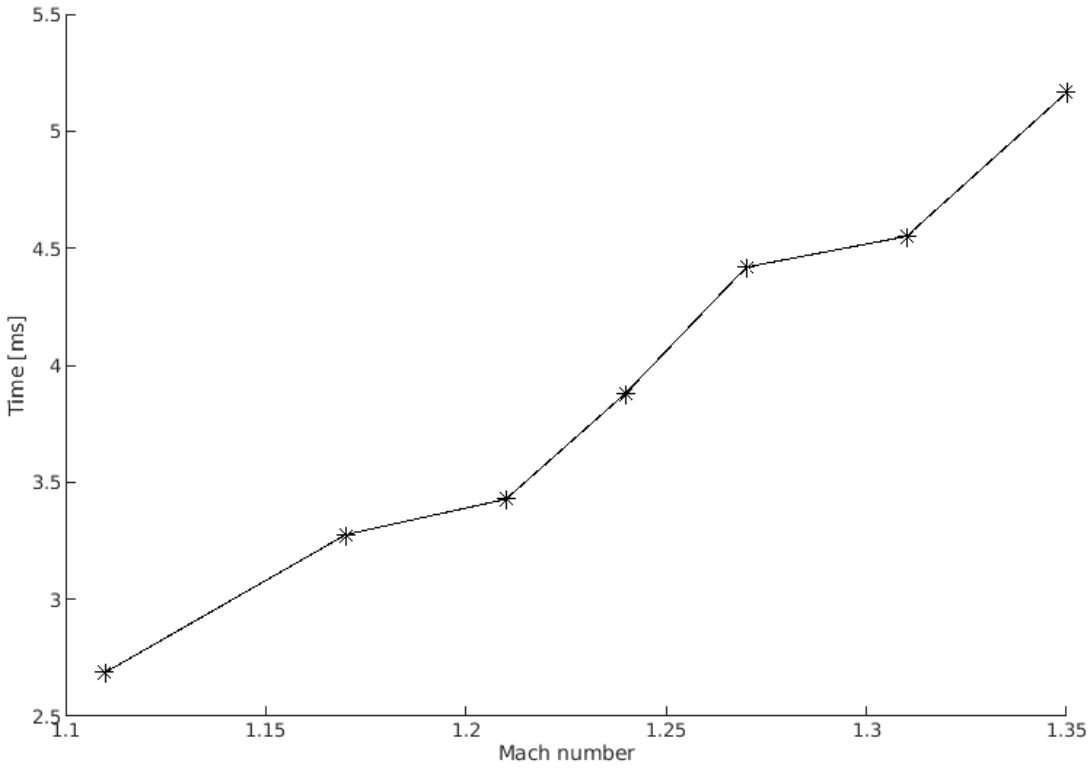


Figure 8.18: Time between incident shock and second shock

layer. The shear layer extends onto the corner of the test piece. The shear layer is visible from Figure 8.19d through to Figure 8.19h as a thick line that extends from the vortex to the corner of the test piece. The slope of the shear layer decreases from Figure 8.19d through to Figure 8.19h. This is contrary to the shock wave diffraction case where the flow is pseudostationary and the angle remains fixed for a given Mach number.

There is another smaller black dot that is formed on the apex of the 90 degree corner just below the shear layer that remains stationary as the diffraction progresses. This is seen in Figure 8.19b and remains in the same position in all the frames that follow through to Figure 8.19h. This black dot was only seen for Mach numbers greater than 1.30. It was not visible for weaker blast waves. This is a viscous vortex. It was observed by B. Skews et al. (2012) in the diffraction of a weak shock wave around a 90 degree corner.

Figure 8.19h shows the contact surface being entrained into the vortex, this is also seen in the subsequent images. However, the contact surface is not visible near the incident shock wave. Figure 8.20 shows the blast wave diffraction around a 90 degree corner at different Mach numbers ranging from Mach 1.11 to Mach 1.44. Similar diffraction features are observed at all Mach numbers. The notable differences are the size of the vortex, the size of the viscous

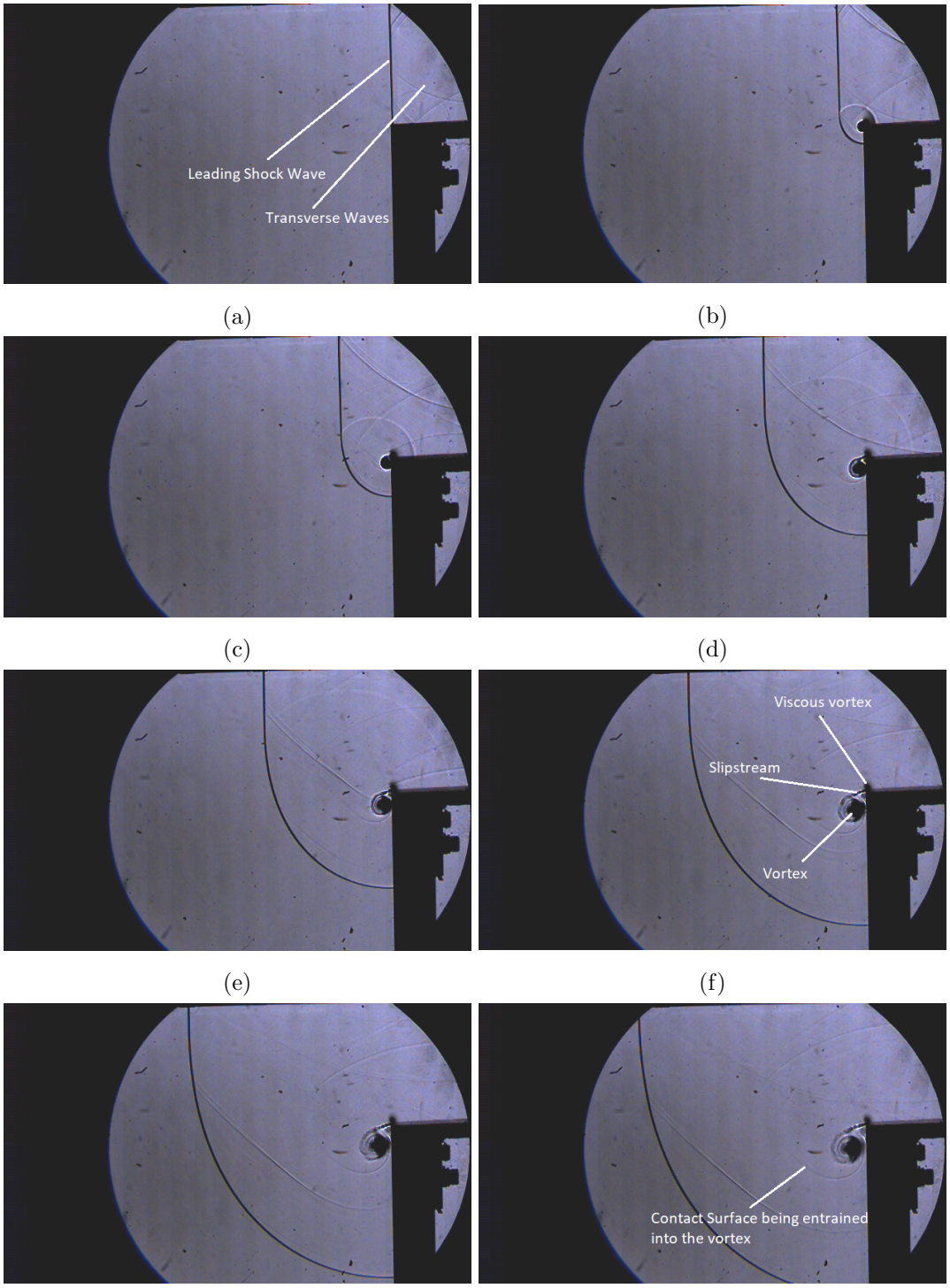
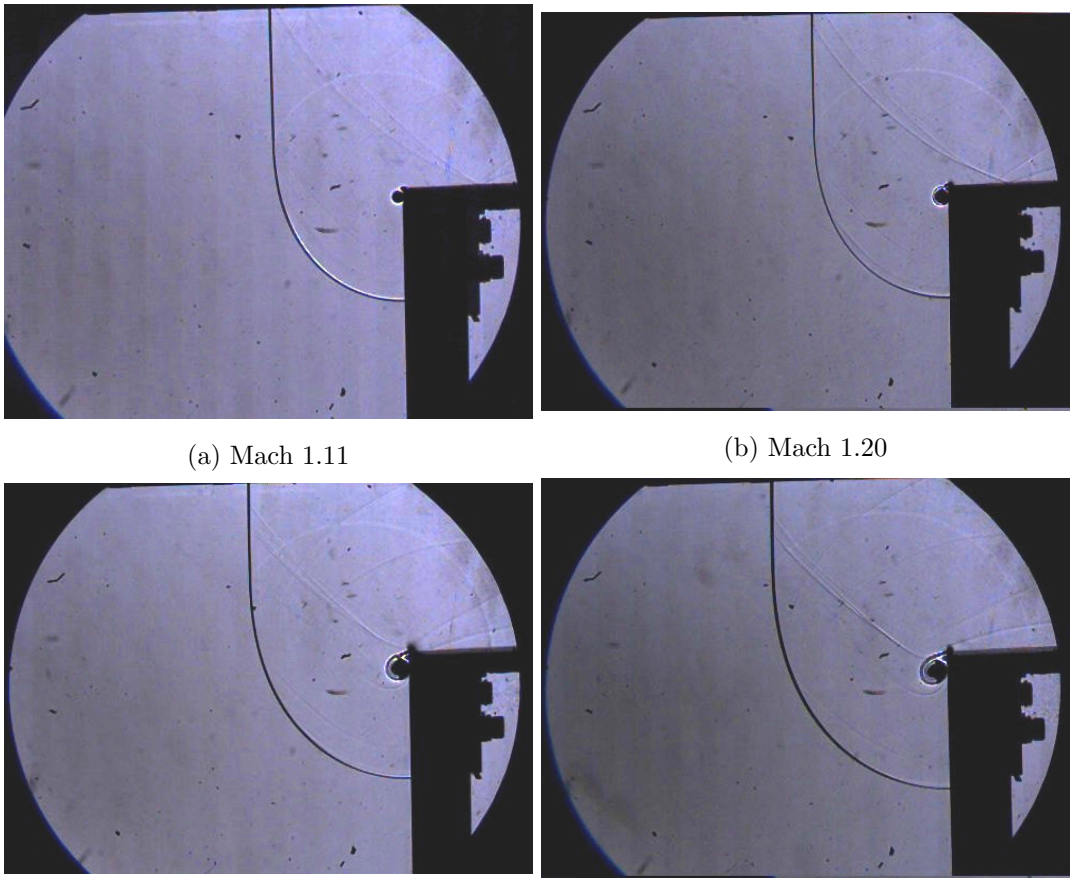


Figure 8.19: Blast wave diffraction around a 90 degree corner for test 5. (Mach 1.35)

vortex and the distances of the each vortex from the corner apex. As the Mach number increases, the vortex grows in size and moves further away from the corner apex. The viscous vortex also grows in size as the Mach number increases and moves higher from the corner apex.



(a) Mach 1.11

(b) Mach 1.20

(c) Mach 1.31

(d) Mach 1.44

Figure 8.20: Blast wave diffraction around a 90 degree corner at different Mach numbers

8.3 Blast wave vs shock wave diffraction

Figure 8.22 shows the ratio of the distance moved by the reflected expansion wave (EW) to the distance moved by the incident shock wave (IS) during the diffraction around a 90 degree corner for both a shock wave and a blast wave at different Mach numbers. The distances were measured from the experimental diffraction images. A line of best fit was fitted to the experimental data to confirm the trend. As the Mach number increases the ratio decreases for both the shock wave diffraction and the blast wave diffraction. The ratio is also higher for the blast waves than for shock waves at a given Mach number.

Both the speed of sound and the flow velocity behind a normal shock wave increase with increasing Mach number. This is shown in Figure 8.24. The increase in the sound speed makes the expansion wave propagate further upstream and the increase in flow velocity makes the expansion wave propagate less further. Figure 8.24 shows that the flow velocity increases at a faster rate than sound speed with increasing Mach number. The overall effect

is that the EW will propagate less further than the IS. This causes the ratio of the distance moved by the EW to the distance moved by the IS to decrease with increasing Mach number.

Figure 8.23 shows the variation of sound speed and flow velocity behind a blast wave. Both the sound speed and flow velocity decay exponentially for a blast wave. For the normal shock wave case, the flow velocity remains at a fixed value depending on the incident Mach number. The faster decrease in flow velocity for a blast wave becomes more pronounced with increasing Mach numbers. This causes a distortion in the reflected expansion head in blast wave diffraction. This is shown in Figure 8.21. The expansion head is circular in the diffraction of weak shock waves. Figure 8.21 shows that the circle is distorted in the blast wave case. This effect is due to the different influence of flow velocity and sound speed. This makes EW travel further for a blast wave diffraction as the Mach number increases. This effect causes the ratio to decrease at a slower rate for blast waves than for shock waves.

At low Mach numbers the EW distance to IS distance ratio for shock waves is similar to the ratio for blast waves in Figure 8.22. As the Mach number decreases the flow velocity decreases and becomes zero at Mach 1. This implies that the propagation of the reflected expansion wave will only be determined by the sound speed. The sound speed is similar for both the shock wave case and the blast wave case. Thus the graphs in Figure 8.22 approach each other as the Mach number approaches unity.

Figure 8.25 shows the variation of blast wind at 1 meter distance from the diaphragm. The velocity of the air behind the blast wave decays from the initial velocity induced by the leading shock wave. The velocity decay continues into the negative region. This implies a reversal in direction of the blast wind. The reversal in direction of the blast wind also occurs in nuclear explosions. This effect further illustrates the realistic nature of the blast waves produced by the blast tube.

The effect of the second shock is evident on the velocity decay profile as a sharp increase in velocity from the negative region.

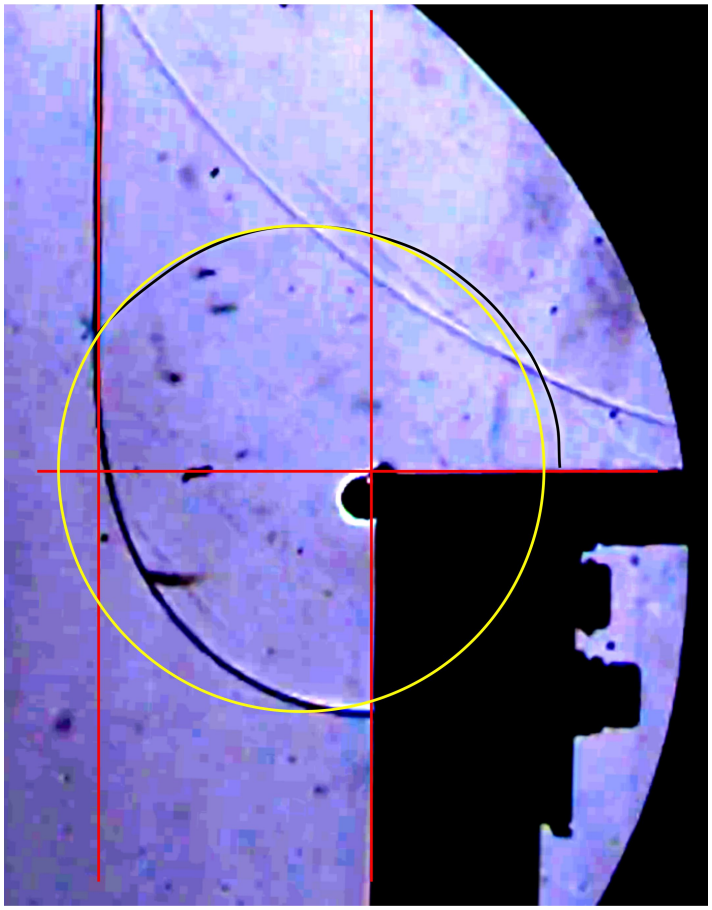


Figure 8.21: Distorted shape of reflected sound wave

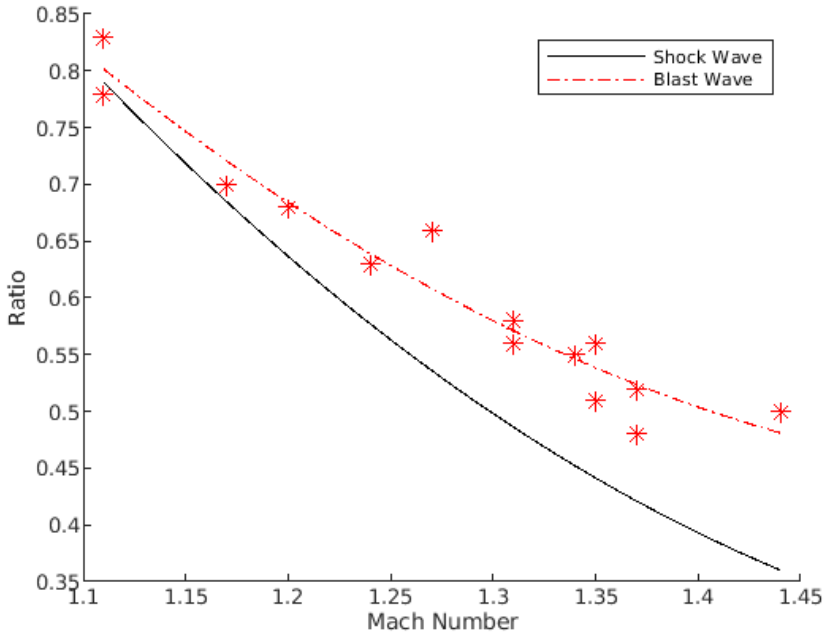


Figure 8.22: Ratio of distance moved by expansion wave to distance moved by incident shock wave from the corner apex

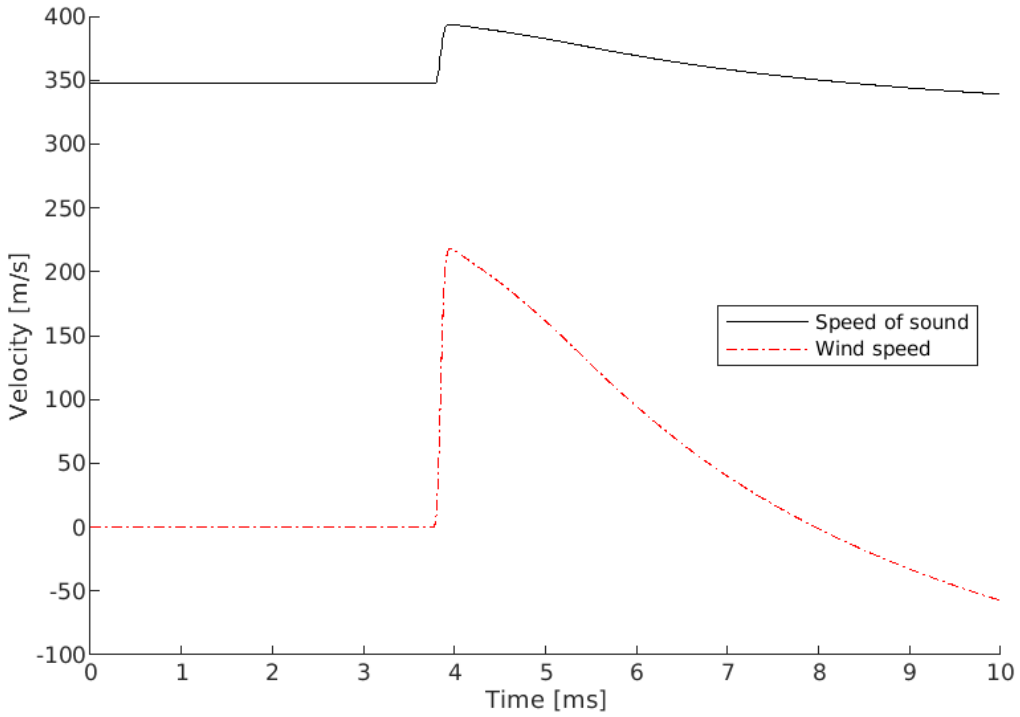


Figure 8.23: Variation of sound speed and flow velocity behind the blast wave (Mach 1.24 nominal)

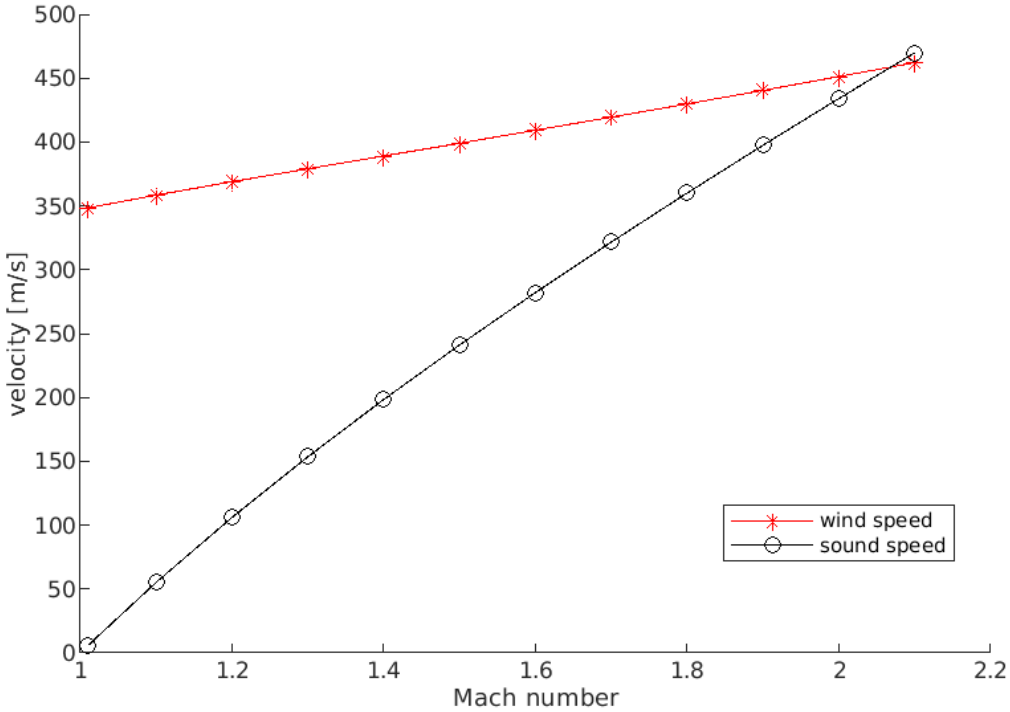


Figure 8.24: Variation of sound speed and flow velocity behind a normal shock wave with increasing Mach number

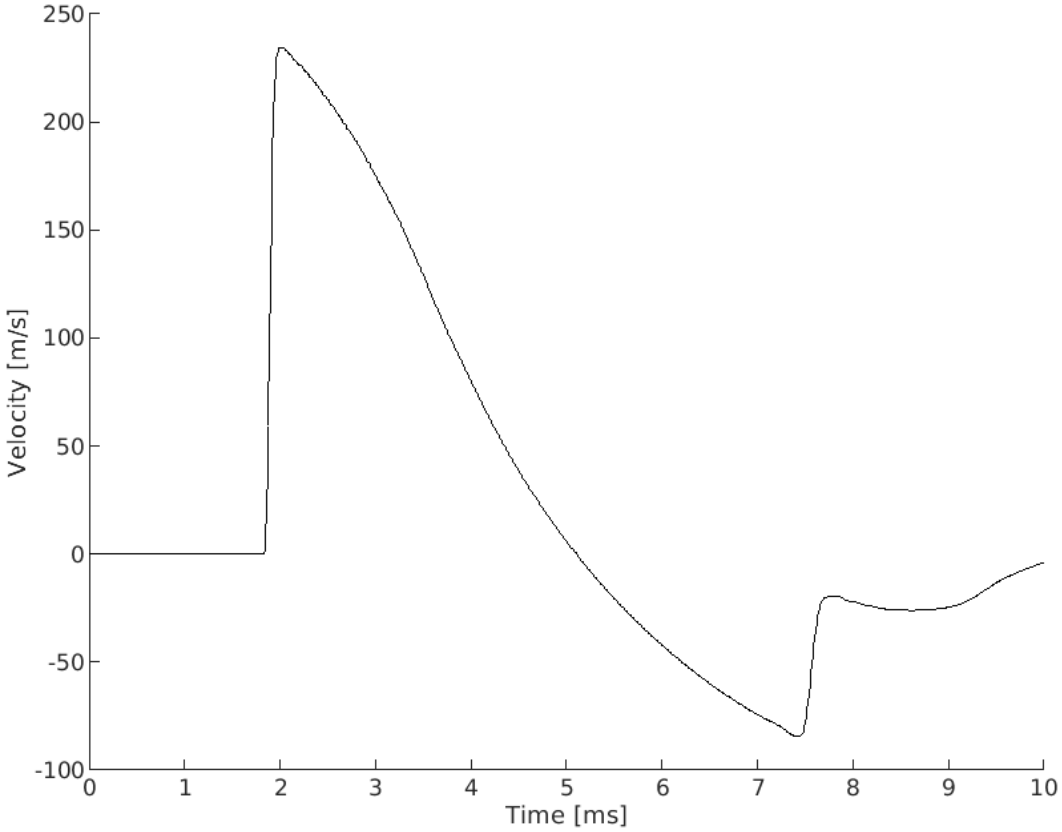


Figure 8.25: Velocity of blast wind at 1m distance from diaphragm

Chapter 9 Conclusions

1. The pressure decay produced by both the numerical and experimental blast tubes showed strong correlation with the Friedlander pressure decay profile. The correlation was validated by comparing the positive impulse for each pressure decay profile. The positive impulse was calculated as the area under the graph in the positive phase. The impulse of the experimental pressure decay profile had a 1.08% difference with the impulse of the Friedlander pressure decay profile. The impulse of the numerical pressure decay profile had a 1.32% difference with the impulse of the Friedlander pressure decay profile. The linearly diverging driver section produces good blast waves with good Friedlander profiles for Mach numbers greater than 1.20.

2. As the Mach number increases, the incident shock wave and the secondary shock wave resulting from the imploding of expansion waves on the corner apex become further apart. This is because the speed of the incident shock wave increases at a faster rate with increasing Mach number than the speed of the secondary shock wave.

3. The perturbed region behind the diffracting blast wave had similar features to the one behind a shock wave at low Mach numbers. This region was characterised by a diffracted shock wave, a reflected expansion wave, a vortex, slipstream and a viscous vortex. The contact surface that is seen in the diffraction of weak shock waves was observed being entrained into the vortex but not visible near the incident shock wave.

4. The reflected expansion wave is circular in the diffraction of weak shock waves. In the blast wave diffraction, the reflected expansion wave was seen to be distorted as soon as it encountered the variable velocity and sound speed behind the diffracting incident shock wave. The ratio of the distance moved by the expansion wave to the distance moved by the incident shock wave decreases for both blast waves and shock waves with increasing Mach number. This is because the distance moved by the incident shock wave increases at a faster rate than the distance moved by the expansion wave with increasing Mach number.

5. The secondary shock wave was observed to remain in the negative phase. This implies that the secondary shock wave will not cause significant structural damage during an explosion compared to the initial shock wave.

6. The ratio of the distance moved by the expansion wave to the distance moved by the incident shock wave for blast waves decreases at a slower rate than for shock waves with increasing Mach numbers. This is because the wind speed behind a blast wave decreases exponentially whereas in the shock wave case the wind speed remains at a fixed value depending on the incident Mach number. The wind behind a blast wave also reverses. These effects overpower the decreasing sound speed. This makes the distance travelled by the expansion wave increase at a faster rate for a blast wave than for the shock wave. This effect causes the ratio to decrease at a slower rate for blast waves than for shock waves.

7. The ratio of the distance moved by the expansion wave to the distance moved by the incident shock wave for blast waves decreases becomes similar to the shock waves ratio at lower Mach numbers. This was because wind velocity tends to zero at Mach 1 and the propagation of the reflected expansion wave will only be determined by the sound speed which will be similar for both the blast wave diffraction and the shock wave diffraction.

Chapter 10 Recommendations

1. High resolution flow visualisation should be used to observe the flow field.
2. An extensive study should be done on the ratio of expansion wave distance to incident shock wave distance for blast waves and shock waves. The resolution of the camera should be increased in this study so that the distances can be measured accurately from the images.
3. A wide range of Mach numbers should be used to study the relationship between the blast waves and shock waves ratio of the expansion wave distance to the incident shock wave distance to confirm the trend.
4. The vortex in the diffraction of blast waves showed complex nature which should be studied in more detail in future studies.

References

Anderson, John David (1990). *Modern compressible flow: with historical perspective*. Vol. 12. McGraw-Hill New York.

Brode, Harold L (1958). *A calculation of the blast wave from a spherical charge of TNT*. Tech. rep. RAND CORP SANTA MONICA CA.

– (1959). 'Blast wave from a spherical charge'. In: *The Physics of Fluids* 2.2, pp. 217–229.

Cullis, IG (2001). 'Blast waves and how they interact with structures'. In: *BMJ Military Health* 147.1, pp. 16–26.

Demby, David Marc (2018). 'Blast wave generation and interactions'. PhD thesis.

Dewey, John M (1964). 'The air velocity in blast waves from TNT explosions'. In: *Proceedings of the Royal Society of London. Series A. Mathematical and Physical Sciences* 279.1378, pp. 366–385.

Friedlander, Frederick Gerard (1946). 'The diffraction of sound pulses I. Diffraction by a semi-infinite plane'. In: *Proceedings of the Royal Society of London. Series A. Mathematical and Physical Sciences* 186.1006, pp. 322–344.

Glass, Irvine Israel (1974). 'Shock waves and man.' In: *Shock waves and man*.

Goel, Manmohan Dass et al. (2012). 'An abridged review of blast wave parameters'. In: *Defence Science Journal* 62.5, pp. 300–306.

Goeller, Jacques et al. (2012). 'Investigation of cavitation as a possible damage mechanism in blast-induced traumatic brain injury'. In: *Journal of neurotrauma* 29.10, pp. 1970–1981.

Karlos, Vasilis, George Solomos and Martin Larcher (2016). 'Analysis of the blast wave decay coefficient using the Kingery–Bulmash data'. In: *International journal of protective structures* 7.3, pp. 409–429.

Merzkirch, Wolgang (2012). *Flow visualization*. Elsevier.

Settles, Gary S and Michael J Hargather (2017). 'A review of recent developments in schlieren and shadowgraph techniques'. In: *Measurement Science and Technology* 28.4, p. 042001.

Settles, GS (2002). *Schlieren and shadowgraph techniques: Visualizing phenomena in transparent media*.

Skews, B. W. (1967). 'The shape of a diffracting shock wave'. In: *Journal of Fluid Mechanics* 29.2, 297304. DOI: 10.1017/S0022112067000825.

Skews, Beric et al. (2012). 'Shear layer behavior resulting from shock wave diffraction'. In: *Experiments in fluids* 52.2, pp. 417–424.

Taylor, Paul A and Corey C Ford (2009). 'Simulation of blast-induced early-time intracranial wave physics leading to traumatic brain injury'. In:

Appendix A Unprocessed Images

This section contains unprocessed data used in the study.

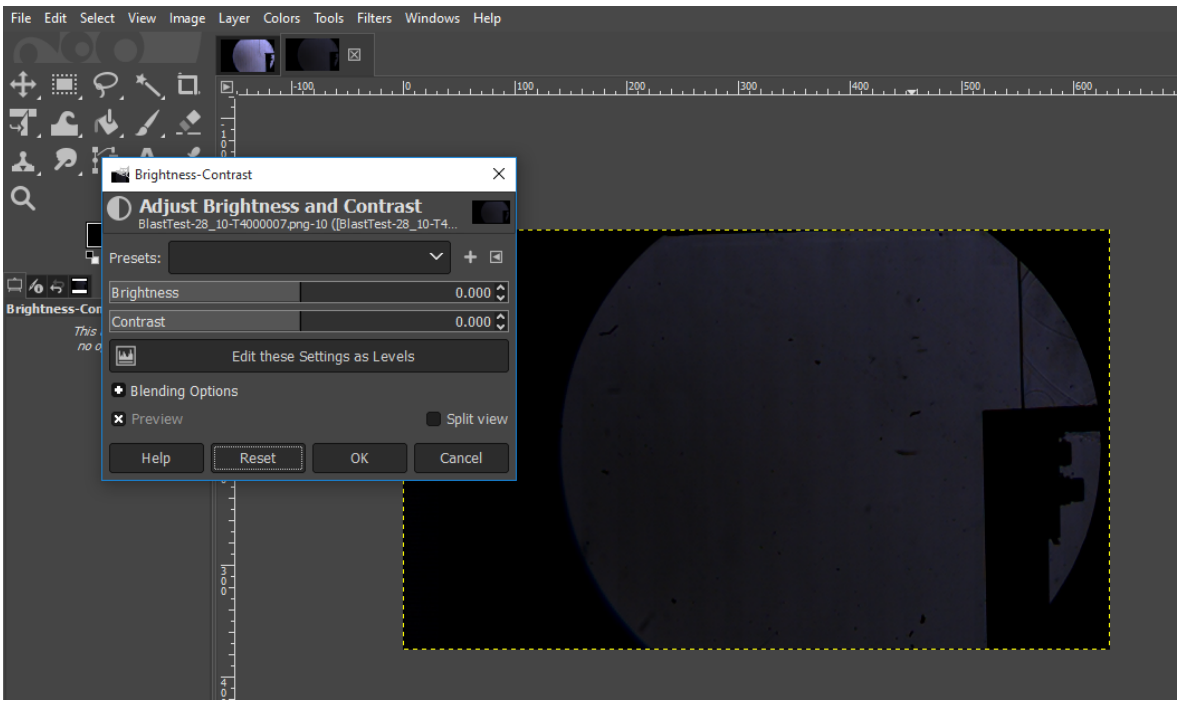


Figure A.1: Image before processing

Appendix B Matlab codes

This section contains the MATLAB codes that were used to process the experimental data and to make the plots in this document.

```
%Blessing Chirewa
%MSc 2019~2021
clc;clear

%%Pressure Transducer Calibration Data
%113B21-SN19620 : 26.75 mV/PSI ~~~ channel 1
%113A21-SN5925 : 31.7 mV/PSI ~~~ channel 2

ch1_factor = 1000/24.75;         %PSI/V
ch2_factor = 1000/24.92;          %PSI/V
psi2kpa = 6.89476;
ch1_factor = ch1_factor*psi2kpa;
ch2_factor = ch2_factor*psi2kpa;



test1_21_10 = csvread('test1_21_10.csv');
P_expt_data = csvread('PressureMach.csv');
cfd_data = csvread('CFDdata.csv');
t_cfd = cfd_data(:,1);
P_cfd = cfd_data(:,2)./1000;
t = test1_21_10(:,1).*7 + 0.003604;
ch1 = test1_21_10(:,2);
ch2 = test1_21_10(:,3);
ch1 = ch1 + ones(size(ch2))*(0-ch1(1));
ch2 = ch2 + ones(size(ch2))*(0-ch2(1));
```

```
P_0 = 1;
td = 0.0025;
ta = 0.00414;
beta = 0.9;

colplot = 4;
P_fd = (P_0*exp(-beta*(t-ta)./td).*(1-((t-ta)./td))).*(t>ta);

P_fd2 = P_fd(P_fd>0);
t_fd2 = t((P_fd>0));
ch1 = ch1.*ch2_factor;
ch2 = ch2.*ch1_factor;
ch1_line = 'k';
ch2_line = ':r';

font = 6;
P_cfd = P_cfd./max(P_cfd);
%ch1 = ch1./max(ch1);

figure(1)
plot(t*1000,ch1,ch1_line,t_cfd*1000,P_cfd,ch2_line,t*1000,P_fd,'-.b',t_fd2*1000,P_fd2,'*r')
legend('Experiment','CFD','Friedlander')
xlabel('Time [ms]')
ylabel('Normalised pressure')
set(gca,'FontName','Times New Roman','FontSize',font)
box('off')
grid('off')
print -depsc graph.eps
saveas(gcf,'test91.png')


figure(3)
plot(t*1000,ch1,ch1_line,t_cfd*1000,P_cfd,ch2_line)
legend('Experiment','CFD')
xlabel('Time [ms]')
ylabel('Normalised pressure')
set(gca,'FontName','Times New Roman','FontSize',font)
box('off')
grid('off')
```

```
print -depsc graph.eps
saveas(gcf,'Pexpt_CFD.png')

figure(4)
plot(t*1000,ch1,ch1_line,t*1000,P_fd,'-.b')
legend('Experiment','FD')
xlabel('Time [ms]')
ylabel('Normalised pressure')
set(gca,'FontName','Times New Roman','FontSize',font)
box('off')
grid('off')
print -depsc graph.eps
saveas(gcf,'Pexpt_FD.png')

figure(5)
plot(t_cfd*1000,P_cfd,ch2_line,t*1000,P_fd,'-.b')
legend('CFD','Friedlander')
xlabel('Time [ms]')
ylabel('Normalised pressure')
set(gca,'FontName','Times New Roman','FontSize',font)
box('off')
grid('off')
print -depsc graph.eps
saveas(gcf,'PCFD_FD.png')


P2 = ch1;

sampleLength = 20;
coeffFilter = ones(1, sampleLength)/sampleLength;

ch1 = filter(coeffFilter, 1, P2);

P2 = ch2;

sampleLength = 20;
coeffFilter = ones(1, sampleLength)/sampleLength;

ch2 = filter(coeffFilter, 1, P2);
```

```
cutting_index = find(t<0.0096);
figure(2)
plot(t(cutting_index)*1000,ch1(cutting_index),ch1_line,'LineWidth',2); hold on;
plot(t(cutting_index)*1000,ch2(cutting_index),ch2_line,'LineWidth',2);hold on;
legend('Channel 1','Channel 2')
xlabel('Time [ms]')
ylabel('Voltage [mV]')
set(gca,'FontName','Times New Roman','FontSize',font)
set(gcf, 'PaperUnits', 'centimeters','PaperPosition', [0 0 15 10])
box('off')
grid('off')
print -depsc graph.eps
saveas(gcf,'Pch1Pch2.png')
hold off;

P1 = Filter(P_expt_data(:,1));
P2 = Filter(P_expt_data(:,2));
P3 = Filter(P_expt_data(:,3));
P4 = Filter(P_expt_data(:,4));
P5 = Filter(P_expt_data(:,5));
P6 = Filter(P_expt_data(:,6));
P7 = Filter(P_expt_data(:,7));
cutting_index2 = find(t>0.004 & t<0.00985);
figure(6)
plot(t(cutting_index2)*1000,Normalise(P1(cutting_index2)),'y',...
    t(cutting_index2)*1000,Normalise(P2(cutting_index2)),':r',...
    t(cutting_index2)*1000,Normalise(P3(cutting_index2)),'-.b',...
    t(cutting_index2)*1000,Normalise(P4(cutting_index2)),'--m',...
    t(cutting_index2)*1000,Normalise(P5(cutting_index2)),'k',...
    t(cutting_index2)*1000,Normalise(P6(cutting_index2)),':c',...
    t(cutting_index2)*1000,Normalise(P7(cutting_index2)),'-.g','LineWidth',1.5);
legend('Mach 1.11','Mach 1.17','Mach 1.21','Mach 1.24','Mach 1.27','Mach 1.31','Mach 1.35')
xlabel('Time [ms]')
ylabel('Normalised pressure')
set(gca,'FontName','Times New Roman','FontSize',font)
set(gcf, 'PaperUnits', 'centimeters','PaperPosition', [0 0 15 10])
box('off')
grid('off')
print -depsc graph.eps
```

```
saveas(gcf,'P_allnormalised.png')
hold off;


PeakVoltages = [0.081569 0.144314 0.156863 0.213333 0.225882 0.263529 0.351373];
Mach = [1.11 1.17 1.21 1.24 1.27 1.31 1.35];

figure(10)
plot(PeakVoltages,Mach,'-*')
xlabel('Peak Voltage [mV]')
ylabel('Mach Number')
set(gca,'FontName','Times New Roman','FontSize',font)
box('off')
grid('off')
print -depsc graph.eps
saveas(gcf,'PMach.png')
hold off;


figure(11)
plot(t*1000,(P_expt_data(:,colplot)-P_expt_data(1,colplot))./(max(P_expt_data(:,colplot)-P_
legend('Experiment Mach 1.21','Friedlander')%,'Mach 1.21','Mach 1.24','Mach 1.27','Mach 1.3
xlabel('Time [ms]')
ylabel('Voltage [mV]')
set(gca,'FontName','Times New Roman','FontSize',font)
box('off')
grid('off')
print -depsc graph.eps
saveas(gcf,'P_allnormalised.png')
hold off;


%%%%%%%%%
INTEGRATION FOR IMPULSE
ch1 = ch1./max(ch1);
t_d = max(t_fd2);
t_a = min(t_fd2);
upper_bound_expt = max(find(t<t_d));
lower_bound_expt = min(find(t>t_a));
```

```
t_int_expt = t(lower_bound_expt:upper_bound_expt);
P_int_expt = ch1(lower_bound_expt:upper_bound_expt);
I_expt = trapz(t_int_expt./1000,P_int_expt);

P_int_FD = P_fd(lower_bound_expt:upper_bound_expt);
I_FD = trapz(t_int_expt./1000,P_int_FD);

upper_bound_cfd = max(find(t_cfd<t_d));
lower_bound_cfd = min(find(t_cfd>t_a));
t_int_cfd = t_cfd(lower_bound_cfd:upper_bound_cfd);
P_int_CFD = P_cfd(lower_bound_cfd:upper_bound_cfd);
I_CFD = trapz(t_int_cfd./1000,P_int_CFD);



X = categorical({'Experiment','Friedlander','CFD'});
X = reordercats(X,{'Experiment','Friedlander','CFD'});
Y = [I_expt I_FD I_CFD];
Y = [I_FD.*1.018243 I_FD I_FD.*1.022943];
exptDiff = (I_expt - I_FD)/I_FD
CFD_Diff = (I_CFD - I_FD)/I_FD
figure(20)
bar(X,Y)
ylabel('Impulse')
set(gca,'FontName','Times New Roman','FontSize',font)
set(gcf, 'PaperUnits', 'centimeters','PaperPosition', [0 0 15 10])
box('off')
grid('off')
print -depsc graph.eps
saveas(gcf,'Impulse.png')
hold off;



x = 0:1/tand(30):38/tand(30);
y = x.*tand(30);
x(end+1) = 100;
y(end+1) = 38;
figure(21)
plot(x,y,'k',x,-y,'k')
```

```
ylabel('height [mm]')
ylabel('length [mm]')

P = (P_expt_data(:,colplot)-P_expt_data(1,colplot));

sampleLength = 10;
coeffFilter = ones(1, sampleLength)/sampleLength;

avgP = filter(coeffFilter, 1, P);
figure(3)
plot(t*1000,[P avgP])




[envHigh, envLow] = envelope(P,16,'peak');
envMean = (envHigh+envLow)/2;

figure(6)
plot(t*1000,P, ...
     t*1000,envHigh, ...
     t*1000,envMean, ...
     t*1000,envLow)

P2 = P;

sampleLength = 20;
coeffFilter = ones(1, sampleLength)/sampleLength;

avgP2 = filter(coeffFilter, 1, P2);
figure(3)
plot(t*1000,[P P2 avgP2])


figure(12)
plot(t*1000,[avgP2])

cutting_index = find(t<0.01);
x0=10;
```

```
y0=10;
width=550;
height=400;

figure(21)
plot(t(cutting_index)*1000,(avgP2(cutting_index)-avgP2(1))./(max(avgP2(:)-avgP2(1))),'k','
plot((t_cfd*1000+0.32927),P_cfd,'-.r','LineWidth',2); hold on;
plot((t(cutting_index)*1000+0.32927),P_fd(cutting_index),':b','LineWidth',2)
legend('CFD','FD')%,'Mach 1.21','Mach 1.24','Mach 1.27','Mach 1.31','Mach 1.35')
xlabel('Time [ms]')
ylabel('Normalised pressure')
set(gca,'FontName','Times New Roman','FontSize',font)
set(gcf, 'PaperUnits', 'centimeters','PaperPosition', [0 0 15 10])
box('off')
grid('off')
print -depsc graph.eps
saveas(gcf,'P_allnormalised.png')
hold off;


figure(22)
plot(t(cutting_index)*1000,[avgP2(cutting_index)],'LineWidth',2)


%%2nd shock arrival time

arrivalTime = [7.09853 7.68642 7.83818 8.29209 8.829209 8.96064 9.57459];
arrivalTime = arrivalTime-4.41064;
MachNum = [1.11 1.17 1.21 1.24 1.27 1.31 1.35];
figure(23)
plot(MachNum,arrivalTime,'*-k')
xlabel('Mach number')
ylabel('Time [ms]')
set(gca,'FontName','Times New Roman','FontSize',font)
set(gcf, 'PaperUnits', 'centimeters','PaperPosition', [0 0 15 10])
box('off')
grid('off')
print -depsc graph.eps
saveas(gcf,'SecondShockTime.png')
```

```
hold off;

function ch1 = Filter(ch1)
 P2 = ch1;

sampleLength = 20;
coeffFilter = ones(1, sampleLength)/sampleLength;

ch1 = filter(coeffFilter, 1, P2);
end

clc;clear;
velocitydata = csvread('velocity.csv');
airspeed_velocity = csvread("Airspeed_and_Velocity.csv");
t_a_v = airspeed_velocity(:,1);
a = airspeed_velocity(:,2);
vs = airspeed_velocity(:,3);
v_diff = a - vs;
tmin = 0.00796;
v1 = -vs.*(t_a_v>tmin);
v2 = vs.*(t_a_v<=tmin);
vs = v1+v2;
Machnum = vs./a;
figure(1)
plot(t_a_v*1000,a,'k',t_a_v*1000,vs,'-.r')
xlabel('Time [ms]')
ylabel('Velocity [m/s]')
legend("Speed of sound","Wind speed","Location","east")
set(gca,'FontName','Times New Roman','FontSize',8)
set(gcf, 'PaperUnits', 'centimeters','PaperPosition', [0 0 15 10])
box('off')
grid('off')
print -depsc graph.eps
saveas(gcf,'airspeedvelocity1.png')
hold off;

t = velocitydata(:,1);
v = velocitydata(:,2);
```

```
tmin = 0.00511;
v1 = -v.*(t>tmin);
v2 = v.*(t<=tmin);
v = v1+v2;
figure(2)
plot(t*1000,Machnum,'k')
xlabel('Time [ms]')
ylabel('Mach number')
set(gca,'FontName','Times New Roman','FontSize',8)
set(gcf, 'PaperUnits', 'centimeters','PaperPosition', [0 0 15 10])
box('off')
grid('off')
print -depsc graph.eps
saveas(gcf,'Machnumber1.png')
hold off;


Ms = [1.01
1.10
1.20
1.30
1.40
1.50
1.60
1.70
1.80
1.90
2.00
2.10];

cs = [5.71
55.20
106.06
153.55
198.39
241.11
282.10
321.68
360.07
```

```
397.47
434.03
469.85
];
vs = [348.4
358.4
368.9
379.0
389.0
399.0
409.2
419.4
429.8
440.4
451.2
462.1
];

figure(3)
plot(Ms,vs,'*-r',Ms,cs,'o-k')
legend('wind speed','sound speed','Location','best')
ylabel('velocity [m/s]')
xlabel('Mach number')
set(gca,'FontName','Times New Roman','FontSize',8)
set(gcf, 'PaperUnits', 'centimeters','PaperPosition', [0 0 15 10])
box('off')
grid('off')
print -depsc graph.eps
saveas(gcf,'v_a_M.png')
hold off;
```